Modelling of laminar diffusion flames with biodiesel blends and soot formation

Anxiong Liu[a,b], Zhan Gao[c,*], Stelios Rigopoulos[b], Kai H. Luo[a,*], Lei Zhu[c]

[a] *Department of Mechanical Engineering, University College London, London WC1E 7JE, United Kingdom*
[b] *Department of Mechanical Engineering, Imperial College London, Exhibition Road, London SW7 2AZ, UK*
[c] *Key Laboratory for Power Machinery and Engineering of M.O.E, Shanghai Jiao Tong University, Shanghai, China*

Abstract

Modelling of soot formation and oxidation of biodiesel fuels is a challenge, due to the complexity of the chemical reactions and soot formation pathways. In this paper, the discretised population balance approach and a PAH-HACA based detailed soot model have been coupled with an in-house CFD code to simulate a laminar diffusion flame with blends of different components of oxygenated biodiesel fuel, and employed to predict combustion performance and soot formation. The simulation aims to reproduce a target experiment which investigated the effects of dibutyl ether (DBE) addition to the biodiesel surrogate (methyl decanoate, MD) by increasing the the mole fraction of DBE from 0 to 40%. A combined and reduced MD-DBE-PAH mechanism developed from three sub-mechanism branches has been employed in the simulation. The simulation results show that temperature rises as the DBE percentage increases to 40%. The swallow-tail shape of the soot occurrence zone and the quantity of soot production are correctly predicted. Regarding the effect of soot suppression, the model has basically captured the reducing tendency of soot formation in the measurements as the DBE addition increases from 0% to 40%. Concentrations of PAHs and C3 species contributing to the formation of aromatic rings are slightly reduced due to the addition of DBE, which is a leading cause of soot suppression. However, on the whole, the numerical solution featured much smaller differences than those observed in the experiment among laminar flames with different MD/DBE ratios, because the combined MD-DBE-PAH mechanism only present a slight difference of concentrations of soot precursor species.

Keywords: biodiesel, methyl decanoate, dibutyl ether, soot suppression, detailed soot model, sectional population balance model

---

1. Introduction

Biodiesel fuel is regarded as renewable energy source in the pathway of going carbon neutral. Vegetation plants, the source of biodiesel, capture the same amount of CO_2 through photosynthesis when growing as is released when biomass is burned. Biodiesel fuel can be blended with petrodiesel in any proportions so that it is compatible with existing diesel engines and distributed combustion infrastructure. The dependence on fossil fuel is reduced as biodiesel fuel can be grown, produced and distributed. The utilisation of biodiesel can also reduce the emissions of total particulate matters, carbon monoxide and unburned hydrocarbons, compared to conventional petro/diesel fuel. Increasingly stringent environmental regulations relating to such emissions, therefore, have prompted a number of study on PM emissions from the combustion of biodiesel and its blends in diesel engines in well-controlled lab-scale flames and reactors [1–8] and diesel engines [9–15].

Most of experimental studies have demonstrated that the addition of biodiesel content has notably decreased PM emissions, compared to long-chain hydrocarbon fuels. For example, Kholghy et al. [4] report that soot formation of a biodiesel surrogate (50%/50% molar ratio of methyl-octanoate/n-decane blends) is lower than n-decane, 1-decene and 5-decene in laminar coflow diffusion flames. Muelas et al. [6] examined in the droplet combustion that a UCO biodiesel (chemical formula $C_{17.32}H_{32.41}O_{1.9}$) and its blends display a much lower propensity to soot formation than

---

[*] Corresponding authors
Email addresses: `gaozhan@sjtu.edu.cn` (Zhan Gao), `k.luo@ucl.ac.uk` (Kai H. Luo)

neat hexadecane ($C_{16}H_{34}$), a major composition of conventional diesel. Iannuzzi et al. [16] and Abboud et al. [3] report that the reduction of soot emissions strongly correlates to the fuel's oxygen content if oxygenated fuel is used. Desjardins et al. [17] has proved the reduction of sooting propensity depends strongly on the oxygenated functional groups: ether, alcohol and ester are in a descending order for soot reduction on the base fuel of pentane (C_5H_{12}). Knothe et al. [18] and Merchan-merchan et al. [2] have concluded that the amount of aromatic compounds are much smaller in biodiesel fuel than in regular diesel, and therefore biodiesel fuel can suppress the soot propensity. However, the existence of unsaturated bonds in the biodiesel molecules adversely enhance the soot formation. For example, Jiang et al. [19] shows the MC ($C_5H_8O_2$, an oxygenated unsaturated ester) blends form about double the amount of soot production than pure C_2H_4 in a laminar coflow flame. Kholghy et al. [4] specifically reports centrally located unsaturation (C=C bond) significantly increases soot formation. McEnally and Pfefferle [20] discussed that doping oxygenateds, e.g., ethanol into ethylene causes a synergistic effect for the promotion of C_3 chemistry.

However, only a very small number of modelling studies have been performed for soot formation with biodiesel fuel. Ni et al. [21] employs an empirical non-precursor model to estimate the soot volume fraction with the filter smoke number (FSN), based on the general purpose CFD software AVL-Fire for diesel engine tests. Arad et al. [22] employed an empirical non-precursor model for the soot nucleation process. Some numerical studies have employed semi-empirical precursor models, correlating precursor species with soot formation processes. For example, An et al. [23] and E et al. [24] assume that the soot nucleation process is a one-step transition from C_6H_2 (a long-chain acetylene) and A_2R_5 (acenapthylene). C_2H_2 (acetylene) is assumed as the precursors for the soot nucleation process [10, 25–28] or surface growth [22, 29, 30], modelled by a chemical reaction with an Arrhenius expression. Some studies also simplify gaseous chemical mechanisms to estimate soot precursor species. For instance, Wang et al. [10] models the formation of soot precursor species (C_2H_2) using a one-step pyrolysis reaction of fuel. Arad et al. [22] employs twelve reactions to model the pyrolysis of a blend of aromatic fuel, aliphatic fuel and ester fuel. In terms of numerical approaches, the two-equation transport approach has been mainly used to solve for two primary variables of soot: the number density / mass fraction of soot [26–28, 31] or the nuclei concentration / mass fraction of soot [22]. In general, soot formation modelling for the combustion of biodiesel fuel (including diesel [32]), is still at the stage of applying empirical/semi-empirical soot kinetics and affordable numerical methods, in the context of complex chemistry and turbulent flows in practical diesel engines.

On the other hand, soot models for the benchmark flames of the International Sooting Flames (ISF) workshop are very detailed and comprehensive, although it is still difficult to obtain quantitative predictions, particularly for turbulent flames. These benchmark flames, which are of concern to the majority of researchers in the soot formation modelling community, involve primarily lightweight hydrocarbon fuel: *i.e.* CH_4 [33], C_2H_4 [34], C_2H_6 [35] in lab-scale conditions, *i.e.* premixed flames, coflow flames and pressurised swirled flames. The soot models applied in benchmark flames, generally include detailed gaseous chemical mechanisms with PAHs pathways, detailed soot processes and aerosol dynamics. Soot processes usually include nucleation (the dimerisation of PAHs [36, 37]), surface growth (HACA mechanism [38] or ARS aromatic site model [39], adsorption of PAHs), multi-regime coagulation/agglomeration [40] and sintering [41], and also the morphology of soot particles. Numerical approaches, including methods of moment, discretisation methods, and Monte Carlos methods, have been implemented to solve properties of soot particles, *i.e.* particle size distribution, the morphology of soot aggregates.

Several challenges need to be identified and addressed in order to close the gap of soot formation models between biodiesel flames and the ISF benchmark flames. First of all, biodiesel fuel is sourced from a variety of vegetation plants and is diverse in terms of chemical components. Researchers have investigated the soot emissions of soybean biodiesel [42], rapeseed biodiesel [43], cooking oil [44], palm oil and rice bran [45]. Generally, the main components of biodiesel are saturated and unsaturated methyl esters with long alkyl chains. A large number of these heavy-molecular components have to be specified by a few species of similar molecular structures. For example, the soybean biodiesel can be modelled as two components - methyl butanoate ($C_5H_{10}O_2$) and n-heptane (C_7H_{16}) by Brakora et al. [46], or as three components - methyl decanoate ($C_{11}H_{20}O_2$), 1,4-hexadiene (C_6H_{10}) and n-dodecane ($C_{12}H_{26}$) by Yu et al. [47], or as four components - methyl decanoate, n-hexadecane ($C_{16}H_{34}$), methyl trans-3-hexenoate ($C_7H_{12}O_2$) and 1,4-hexadiene [48]. As a result, a large variety of biodiesel fuel and the uncertainty of chemical compositions lead to a difficulty in formulating benchmark flames for biodiesel combustion and emissions.

Second, researchers prefer to study the blending of different types of biodiesel fuel to optimise the combustion performance and emission reduction. Therefore, different sub-mechanisms of reaction kinetics and chemical/physical properties should be considered in order to form a detailed chemical mechanism with soot precursor species. Errors occur when the connections of different chemical databases are not well coordinated, particularly when the chemical concentrations of components cannot be fully validated in the measurements. This viewpoint will be elaborated later in this article.

Third, detailed soot formation models with a series of parameters have been calibrated for ISF benchmark flames with lightweight hydrocarbon fuels. The more elaborate a soot model is, the more parameters should be calibrated, *i.e.* the collision efficiency of the PAH dimerisation for the nucleation process [36], the active site ratio in the HACA mechanism [37] or the ARS aromatic site model [49] for the surface growth rate, the particle sintering time [41] and the morphology description of soot aggregates [49, 50]. Some of the sub-models are based on soot precursor species (*i.e.*, C_2H_2, PAH), and very sensitive to the gaseous chemical mechanisms [50].

Prior to this study, researchers have explored co-flow diffusion flames, using the methane/ethylene base added with the biodiesel fuel [51–53], or using gasoline / diesel / long-chain hydrocarbons added with biodiesel fuel [45, 54, 55]. The added biodiesel fuel was basically a pure component of alcohols, esters or ethers. The aim of the article is to model the soot formation in flames with the blended fuel of different oxygenated surrogates using detailed soot kinetics. The target experiment in this study was conducted by Gao et al. [5]. In the experiment, dibutyl ether ($C_8H_{18}O$, DBE) was added to the base fuel of methyl decanoate ($C_{11}H_{22}O_2$, MD), a major component in many types of biodiesel fuel. When the mole fraction of DBE in the fuel stream rises from 0% to 40%, the soot formation is largely suppressed. The main task of this paper is to employ a recently developed conservative method for solving the population balance equation [56], coupled with an in-house CFD code (BOFFIN) [57] with a comprehensive chemical mechanism and transport properties, to predict soot formation in a laminar diffusion flame with biodiesel blends. A detailed soot model, of which the parameters are consistent with an application in one of the ISF benchmark flames, will be used in this simulation. The main challenge is to form a proper combined gas-phase chemistry including various necessary oxygenated surrogates and to propose a detailed soot kinetics to capture the soot suppression effect. Main error sources of the discrepancy between the simulations and target measurements will be offered.

2. Simulation and experiment setup

2.1. The Co-flow flame burner and simulation cases

In the experiment, the burner consisting of three concentric brass tubes is shown in Fig.1a. The central tube supplies the mixture of fuel: methyl decanoate (MD), dibutyl ether (DBE) and carrier gas N_2. The intermediate tube is used to supply co-flow air stream with the flow rate (8.43 L/min). The outer tube supplies N2 (16.2 L/min) as a shield to protect flames from the the surrounding air. The inner diameters of three tubes are 10, 26 and 59 mm, respectively. The fuel and the burner were heated at 573 K to keep the fuel above the boiling point. Air and the protecting gas were preheated to $473\,\mathrm{K}$. In the experiment, the carbon atom flow rates for all the fuel blends remain constant at 6 g/h. Compositions of the fuel stream in three flames are presented in Table 1.

Blended fuel	Components (mol %)		Flow rate		
	MD	DBE	blend fuel [g/h]	Carbon atom flow rates [g/h] / [mol/h]	carrier gas N_2 [L/h]
Pure MD	100	0	8.45		
70% MD	70	30	8.38	6.0 / 0.5	5.82 (473 K)
60% MD	60	40	8.35		

Table 1: The simulation cases: fuel components and mass flow rates

The experimental apparatus is completely described in [5]. Temperature profiles in flames were measured by the rapid thermocouple insertion technique and the soot volume fraction was performed by the 2D LII measurement, which were quantitatively calibrated against the high spatial resolution laser cavity extinction measurement [58].

2.2. Numerical methods for the reacting flow and soot formation

The population balance equation (PBE) is a rigorous way to solve the particle size distribution in aerosol dynamics. In the present article, the discretised PBE with a conservative finite volume scheme [56] considers the processes of convection, thermophoresis, diffusion, nucleation, growth and coagulation, which is written as

$$\begin{aligned}
&\frac{\partial n(v;\mathbf{x},t)}{\partial t} + \sum_{j=1}^{3} \frac{\partial\left((u_j+U_j^{\mathrm{T}})n(v;\mathbf{x},t)\right)}{\partial x_j} + \frac{\partial\left(G(v)n(v;\mathbf{x},t)\right)}{\partial v} \\
&= -\sum_{j=1}^{3} \frac{\partial K_j(v;\mathbf{x},t)}{\partial x_j} + \dot{B}(\mathbf{Y})\delta(v-v_0) \\
&+ \frac{1}{2}\int_0^v \beta(v-v',v')n(v-v',\mathbf{x},t)n(v',\mathbf{x},t)\,dv' - \int_0^\infty \beta(v,v')n(v,\mathbf{x},t)n(v',\mathbf{x},t)\,dv',
\end{aligned} \tag{1}$$

Here, the number density $n(v;\mathbf{x},t)$, corresponds to the number of particles with volume in $[v, v+dv]$ at the location x and time t per unit of physical space, referred as the particle size distribution. And $G(v)$ is the combined surface growth and oxidation rate, $\dot{B}$ represents the nucleation rate, v_0 is the nuclei volume and $\beta(v,v')$ denotes the coagulation kernel. $K_j(v,\mathbf{x},t)$, moreover, represents the diffusive flux of number density along the j^{th} coordinate direction in physical space and $\mathbf{U}^{\mathrm{T}}$ represents the thermophoretic velocity. The soot kinetics will be described in Section 2.4.

The discretised PBE is coupled with the continuity, Navier-Stokes, energy and species transport equations to simulate combustion with soot formation. The transport equations of species and energy in the complete form are described as Eq. 2 and Eq. 3, respectively,

$$\frac{\partial \rho Y_k}{\partial t} + \frac{\partial}{\partial x_j}\left(\rho u_j Y_k\right) = \underbrace{\frac{\partial}{\partial x_j}\left[\rho D_{km}\frac{\partial Y_k}{\partial x_j}\right]}_{\text{Ordinary diffusion}} + \dot{\omega}_k + \underbrace{\frac{\partial}{\partial x_j}\left[\rho D_{km} Y_k \frac{\partial(\ln \bar{W})}{\partial x_j}\right]}_{\text{Molecular Weight}} + \underbrace{\frac{\partial}{\partial x_i}\left(D_k^{\mathrm{T}}\frac{\partial(\ln T)}{\partial x_i}\right)}_{\text{Thermophoresis}} \tag{2}$$

where Y_k and X_k are the mass fraction and mole fraction of the species k, respectively. D_{km} is the molecular diffusion coefficient of species k in the multi-component mixture, while D_K^{T} is the thermal diffusion coefficient. W_k and $\bar{W}$ are the molecular weight of species k and the local average molecular weight, respectively.

$$\begin{aligned}
\frac{\partial \rho h}{\partial t} + \frac{\partial}{\partial x_j}\left(\rho u_j h\right) &= \underbrace{\frac{\partial}{\partial x_j}\left(\rho D\frac{\partial h}{\partial x_j}\right) - \sum_k \frac{\partial}{\partial x_j}\left[\rho(D-D_k)h_k\frac{\partial Y_k}{\partial x_j}\right]}_{\text{Ordinary differential diffusion}} \\
&+ \underbrace{\frac{\partial}{\partial x_j}\left[\rho Y_k D_k h_k \frac{\partial(\ln W_k)}{\partial x_j}\right]}_{\text{Molecular Weight}} + \underbrace{\frac{\partial}{\partial x_j}\left[\rho Y_k D_k^{\mathrm{T}} h_k \frac{\partial(\ln T)}{\partial x_j}\right]}_{\text{Thermophoresis}} + \underbrace{\frac{\partial}{\partial x_j}\left(\sum_k \frac{RT}{W_k X_k} D_k^{\mathrm{T}}\frac{\partial X_k}{\partial x_j}\right)}_{\text{Dufour effect}} + \dot{Q}_r
\end{aligned} \tag{3}$$

where h and h_k are the total enthalpy and specific enthalpy of species k, respectively. D is the heat transfer coefficient. All these thermodynamic and transport parameters are formulated in the same way as Chemkin Pro [59]. In order to account for the reduction of mixture enthalpy due to radiation $\dot{Q}_r$ by gas phase molecules and soot, we include a radiation model based on the assumption of optical thinness [60]. Here, the temperature dependence of the Planck mean absorption coefficients is approximated by polynomials [61].

When the local average molecular weight does not vary significantly throughout the reacting flow field, the diffusion term with respect to molecular weight can be neglected. Meanwhile, the thermal diffusion coefficient D_k^{T} is also dependent on the difference of molecular weights between species so that thermophoresis term is also neglected when the local average molecular weight remains unchanged. In that situation, the convection term and diffusion term in regard to a scalar can coexist in the numerical implementation of an implicit scheme instead of many additional terms with an explicit scheme, thus improving the computational stability.

$$\frac{\partial \rho \phi_k}{\partial t} + \frac{\partial \rho u_j \phi_k}{x_j} = \frac{\partial}{\partial x_j}\left[\rho \Gamma_k \frac{\partial \phi_k}{\partial x_j}\right] \tag{4}$$

where ϕ_k is any scalar and Γ_k is the diffusion coefficient.

However, in the simulation of laminar diffusion flames with biodiesel fuels, the local average molecular weight varies notably and the additional diffusion terms make a difference (see Appendix C): the mass diffusion term should be expressed in terms of mole fraction in the transport equations of species and energy. Therefore, the complete forms are employed in this article (Eq. 2 and Eq. 3).

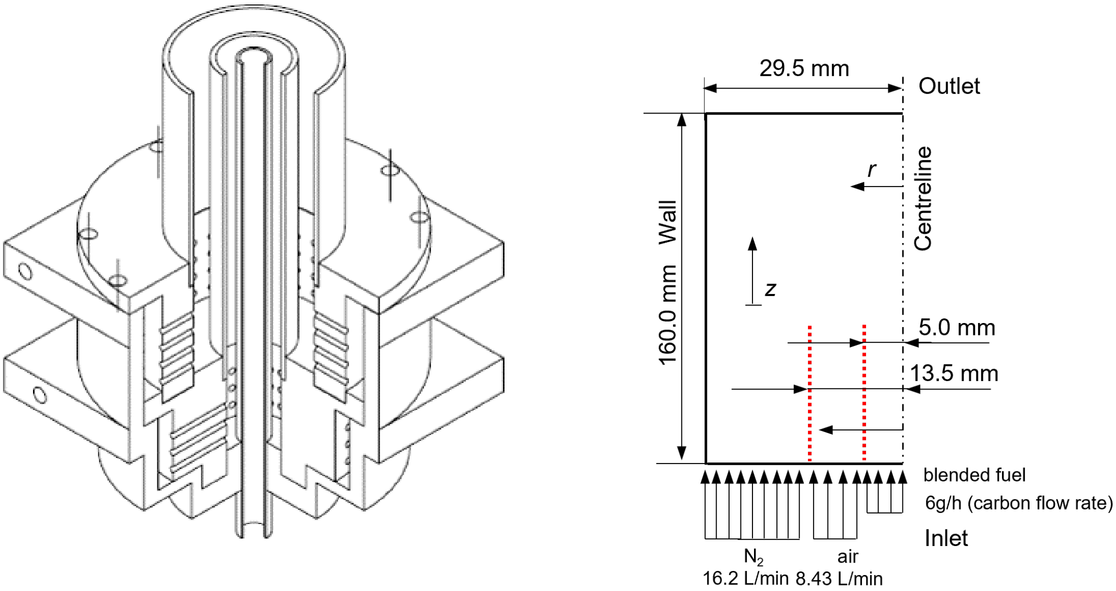

(a) Burner consisting of three concentric brass tubes

(b) Computational domain

Figure 1: Configuration of the burner and the computational domain

2.3. Gaseous chemical mechanism

To gain insight into the process of soot formation in the laminar flame with blended fuels of MD and DBE, a comprehensive chemical mechanism including the combustion of MD and DBE, and PAHs formation is required. However, as the target experiment was the first attempt to study the combustion behaviours of MD-DBE mixture, a well-validated mechanism of MD-DBE cannot be found. In addition, PAHs pathways should also be incorporated in order to model soot formation. Therefore, three sub-mechanisms, respectively, of MD by Sarathy et al. [62], of DBE by Cai et al. [63], and of PAHs by Blanquart and Pitsch [36] will be combined. Another dilemma is faced that systematic measurements of concentrations of key gas species for the MD-DBE mixture combustion in the lab-scale reactors or flames do not exist, thus an alternative but convincing approach to validate the combined MD-DBE-PAH mechanism is proposed below. Here, simulation results of the MD mechanism [62] for the stoichiometric MD-air combustion and the DBE mechanism [63] for the stoichiometric DBE-air combustion in a perfect stirred reactor (PSR) are selected, as *ad-hoc* references for further validation, because both mechanisms have been validated in the respective experiments [62, 63].

The MD mechanism [62], consisting of 648 species and 2998 reactions, reproduces the behaviour of its original detailed mechanism in plugflow and stirred reactors for temperatures of 900 – 1800 K, equivalence ratios of 0.25 – 2.0, and pressures of 1 and 10 bar. This mechanism also well predicts the test data in opposed-flow diffusion flames. The oxidation kinetics of DBE Cai et al. [63], consisting of 328 species and 2236 reactions, was validated in the measurement of ignition delay times and laminar flame speeds in a laminar flow reactor. The sub-mechanism in [64], adopted in the soot modelling of ethylene diffusion flames [50], still accounts for the PAH pathways.

As both the full MD and DBE sub-mechanisms are comprised of a large number of species, they should be simplified for the flame simulation. Using the DRGEPSA (Directed Relation Graph with Error Propagation and Sensitivity Analysis) method in the commercial software CHEMKIN PRO, the species shared by the MD, DBE, and PAH sub-mechanisms are selected as the target species for mechanism reduction. The relative tolerance errors for target species range from 10% - 20%, listed in Appendix A. Figure 2 compares the reduced mechanisms with the corresponding full mechanisms for the stoichiometric MD-air and DBE-air combustion, respectively, in a PSR simulation. The mechanisms of full MD, full DBE, reduced MD and reduced DBE are marked as 'F_M', F_D', 'R_M', 'R_D'. It is clear that the reduced mechanisms have replicated the temperature profiles by the full mechanisms, which means ignition delay times are accurately predicted. Mole fractions of major species (OH, H, CO),C_2H_2 and the minor species for PAHs formation (C_3H_3, C_3H_4) by the reduced mechanisms and full mechanisms coincide.

The combination of various chemical mechanisms is a complicated task. The common species with different names in the three mechanism branches are unified first. The most tricky part is to choose the chemical rate constants of common reactions and the thermochemical properties of common species from different sub-mechanisms. For example, the reduced mechanisms of MD and DBE are combined in two ways: (1) all the chemical rates and thermochemical properties from the MD reduced mechanism (R_M) are maintained, combined with other reactions and species of the DBE reduced mechanism (R_D); (2) on the opposite, the DBE reduced mechanism (R_D) lays the foundation, other reactions and species from MD full mechanism (R_M) are added in. These two combined mechanisms are labelled as CR_MD and CR_DM, respectively. However, Figure 2 also shows that neither of these combined mechanism is accurate in the PSR simulation in two separate stoichiometric conditions: MD-air mixture and DBE-air mixture. A major problem for the CR_MD mechanism is that ignition delay times are longer in both conditions: the maximum temperature and peaks values of major species (OH, C_2H_2, H and CO) appear later than the full mechanisms. Another problem for both combined mechanisms is in the prediction of PAHs precursor species, C_3H_3 and C_3H_4: in the MD-air combustion, the CR_DM mechanism underestimated the PAH precursor species by about 2/3 of its standard values (prediction by the F_M mechanism), while the CR_MD mechanism performs much better, with a nearly accurate C_3H_4 profile. On the opposite, in the DBE-air combustion, the CR_DM mechanism obtains accurate profiles while the CR_MD mechanism overpredicts the mole fractions of C_3H_3 and C_3H_4 by around 1 - 2 times.

Unfortunately, the combined mechanisms fail to capture the combustion features of the added fuels. Therefore, a way should be considered to neutralise the 'partiality' of combined mechanisms: now starting from the CR_DM mechanism because it accurately preserves the ignition delay times in both combustion mixtures, it is then combined with the PAH sub-mechanism: all the chemical rates and thermochemical properties from the CR_DM mechanism are kept, combined with other reactions and species of the PAH sub-mechanism. Now, the reaction rates of common reactions are manually switched related to the monitored C_2H_2, C_3H_3, C_3H_4, C_3H_5 from three different sub-mechanisms. Appendix B summarises the reaction rates of common reactions inherited from the F_M mechanism or the PAH sub-mechanism, instead of the prioritised F_D mechanism. Finally, the adjusted combined MD-DBE-PAH mechanism, labelled as CRA_DMBpp mechanism, is concluded, with 530 species and 3437 chemical reactions. Figure 2 also displays its performance in the PSR combustion. The CRA_DMBpp mechanism accurately captures the ignition delay times and concentrations of a majority of species. The only evident discrepancy is in the profile of C_3H_3, which is about 1/3 reduction of the peak value than the F_M reference in Fig. 2a, but it is still superior to the results of CR_MD and CR_DM mechanisms.

As the PAH formation is critical to soot formation, other chemical mechanisms for the PAH formation sub-mechanism are also refered in this study. The DLR mechanism proposed by Dworkin et al. [65] includes 97 gas species and 831 chemical reactions and has been validated for zero- and one-dimensional premixed flame systems. Slavinskaya and Frank [66] and then extended to a sooting ethylene/air diffusion flame in a coflow geometry [65]. By combining the DLR mechanism with the 'CR_DM' mechanism, and the overlapped chemical rates and thermochemical properties from the mechanism 'CR_DM', the formed mechanism 'CRA_DMDlr', similar to the combined and reduced mechanism 'CRA_DMBpp', also underpredicts C_3 species in the stoichiometic MD-air mixture combustion (see Fig. 2a) with respect to the standard profiles of the full mechanism 'F_M', and achieves a good agreement of soot precursor species C_2H_2 and C_3 species in the stoichiometic DBE-air mixture combustion.

As the PAH species are the major precursors for soot formation modelling, Fig. 2 shows how the concentrations of PAHs are affected as the mechanism 'CR_DM' is combined with the BPP and DLR mechanisms. As the PAH species are not included in the full MD (F_M) and DBE (F_D) mechanisms, a rich ethylene-air combustion in the homogeneous reactor is considered to compare the performance of the combined mechanisms 'CRA_DMBpp' and 'CRA_DMDlr', with the full PAH mechanisms BPP (F_Bpp) and DLR (F_Dlr). In fact, the BPP and DLR mechanisms show different predictions of the temperature profile and the soot precursors: C_2H_2, C_3 and PAHs. The combined mechanisms actually underpredict the soot precursor species, compared with their own full mechanism. This is because the carbon species flows into the added branch 'CRA_DM'.

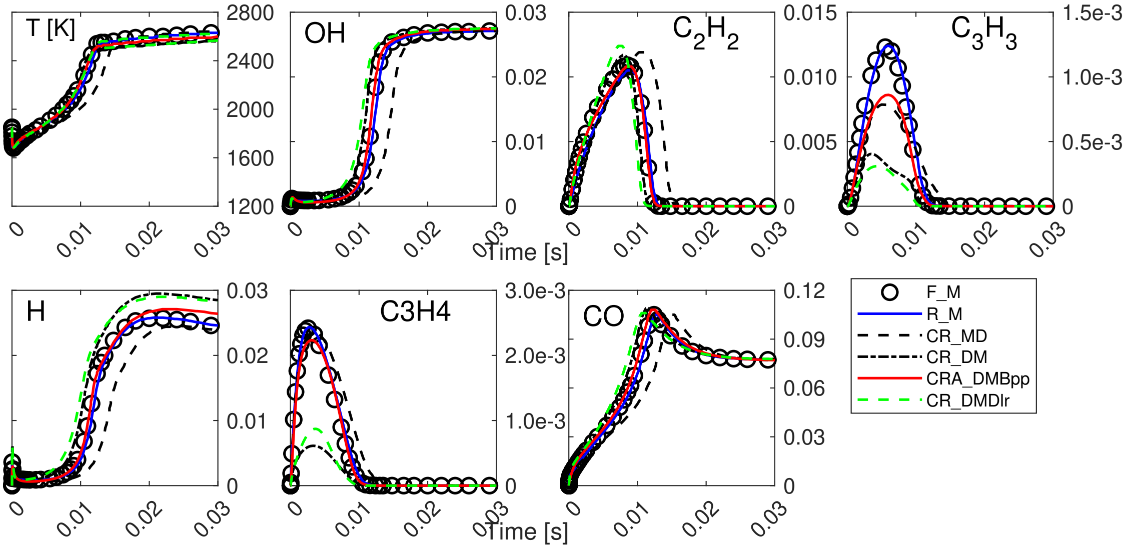

(a) stoichiometric MD-air mixture

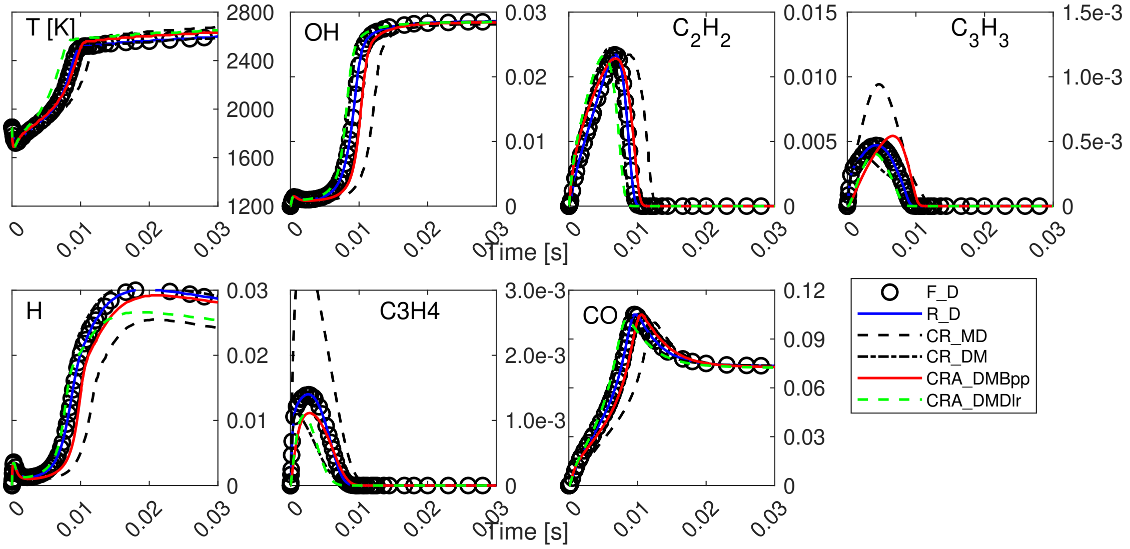

(b) stoichiometric DBE-air mixture

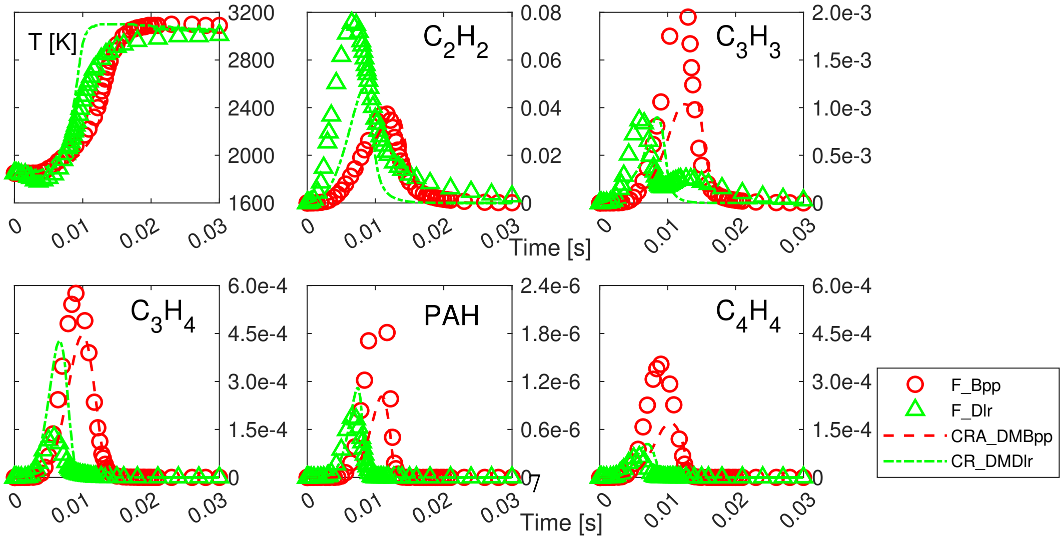

(c) Ethylene-air mixture ($\phi = 2$)

Figure 2: Comparison of the simulations with full mechanisms (labelled as F), the reduced mechanism (labelled as R), combined-reduced mechanisms (labelled as CR), the adjusted combined-reduced DBE-MD-PAH mechanism (labelled as CRA) in a perfect stirred reactor

2.4. *Soot kinetics model*

The population balance equation (PBE) is a statement on the balance of number density in $(v, \mathbf{x})$-space, with respect to source and sink processes for the creation and removal of number density [67]. At $(\mathbf{x}, t)$, $n(\cdot, \mathbf{x}, t)$ is often referred to as the particle size distribution. Considering soot nucleation and aggregation as source/sink processes, the PBE is given by

$$\frac{\partial n(v,\mathbf{x},t)}{\partial t} + \sum_{j=1}^{3} \frac{\partial\left((u_j + U_j^{\mathrm{T}} + K_j) n(v,\mathbf{x},t)\right)}{\partial x_j} + \frac{\partial\left(G(v,\mathbf{Y}) n(v,\mathbf{x},t)\right)}{\partial v} = \dot{B}(\mathbf{Y})\delta(v - v_0)$$
$$+ \frac{1}{2}\int_0^v \beta(v-w,w) n(v-w,\mathbf{x},t) n(w,\mathbf{x},t)\,\mathrm{d}w - \int_0^\infty \beta(v,w) n(v,\mathbf{x},t) n(w,\mathbf{x},t)\,\mathrm{d}w, \quad (5)$$

where $G(v, \mathbf{Y})$ is the combined surface growth and oxidation rate, $\dot{B}$ represents the nucleation rate, v_0 is the nuclei volume and $\beta(v, w)$ denotes the aggregation kernel. $K_j(v, \mathbf{x}, t)$, moreover, represents the diffusive velocity the jth coordinate direction in physical space,

$$K_j(v,\mathbf{x},t) = -\frac{D_{\mathrm{p}}(v,\mathbf{x},t)}{n(v,\mathbf{x},t)} \frac{\partial n(v,\mathbf{x},t)}{\partial x_j}, \quad (6)$$

and $D_{\mathrm{p}}(v, \mathbf{x}, t)$ represents the kinematic diffusivity of a particle with volume v [68]. $D_{\mathrm{p}}(v, \mathbf{x}, t)$ is controlled by the diameter $d_{\mathrm{p}}(v)$ of spherical particles, or the hydrodynamic diameter $d_{\mathrm{h}}(v)$ for aggregates, as indicated in investigations on the dynamic properties of polymers suspended in a solvent [69].

In the spatial convection term of Eq. (5), $\mathbf{U}^{\mathrm{T}}(v, \mathbf{x}, t)$ represents the thermophoretic velocity that a particle immersed in a flow with temperature gradients experiences. Depending on the Knudsen number Kn, the thermophoretic velocity is computed for the free-molecular ($\mathrm{Kn} > 10$), transitional ($0.1 < \mathrm{Kn} < 10$) or continuum regimes ($\mathrm{Kn} < 0.1$) [70],

$$U_j^{\mathrm{T}} = \begin{cases} -\dfrac{3\nu}{4\left(1 + \frac{\pi\alpha_{\mathrm{m}}}{8}\right)} \dfrac{1}{T}\dfrac{\partial T}{\partial x_j}, & 10 < \mathrm{Kn} \\ -\dfrac{2C_{\mathrm{s}}\nu\left(\frac{k_{\mathrm{g}}}{k_{\mathrm{p}}} + C_{\mathrm{t}}\mathrm{Kn}\right)}{(1 + 2C_{\mathrm{m}}\mathrm{Kn})\left(1 + \frac{2k_{\mathrm{g}}}{k_{\mathrm{p}}} + 2C_{\mathrm{t}}\mathrm{Kn}\right)} \dfrac{1}{T}\dfrac{\partial T}{\partial x_j}, & 0.1 < \mathrm{Kn} < 10 \\ 0, & \mathrm{Kn} < 0.1 \end{cases}, \quad (7)$$

where the accommodation factor α_{m} is set to 0.9.

Soot formation processes involve PAHs nucleation, surface growth by adding hydrocarbon species, and coagulation between spherical particles and fractal aggregates. The soot particle nucleation step is considered as the coalescence of two PAH molecules of same species and the collision frequency is given by

$$\dot{B}(\mathrm{PAH}_i) = 4\gamma_i N_{\mathrm{A}} d_i^2 \sqrt{\frac{\pi R_{\mathrm{J}} T}{M_i}} [\mathrm{PAH}_i]^2, \quad (8)$$

where R_{J} indicates the gas constant (in $[\mathrm{kmol} \cdot \mathrm{K/kJ}]$), N_{A} is the Avogadro's number, d_i is the diameter of molecules PAH_i and M_i, represents the molar mass of PAH_i [kg/kmol]. The PAH species and dimerisation efficiencies γ_i are given in Table 2 [36].

The hydrogen abstraction acetylene addition (HACA) mechanism contributes to the growth of benzenoid polycyclic aromatic hydrocarbons (PAHs) and soot particles, which is modelled as the following reversible reactions on the $\mathrm{C_{soot}}\cdot$ (radical sites on dehydrogenated carbon atoms) and the reactive sites $\mathrm{C_{soot}}$-H (sites bonding hydrogen atoms and carbon atoms):

$$\mathrm{C_{soot}} - \mathrm{H} + \mathrm{H} \quad \Leftrightarrow \quad \mathrm{C_{soot}}\cdot + \mathrm{H_2}$$
$$\mathrm{C_{soot}} - \mathrm{H} + \mathrm{OH} \quad \Leftrightarrow \quad \mathrm{C_{soot}}\cdot + \mathrm{H_2O}$$

Species	Molar mass M_i [kg/kmol]	Name	Collision efficiency γ_i
$C_{10}H_8$	128.17	Naphthalene	0.0010
$C_{12}H_8$	152.20	Acenaphthylene	0.0030
$C_{12}H_{10}$	154.21	Biphenyl	0.0085
$C_{14}H_{10}$	178.24	Phenathrene	0.0150
$C_{16}H_{10}$	202.26	Pyrene	0.0250
		Acephenanthrylene	0.0250
		Fluoranthene	0.0250
$C_{18}H_{10}$	226.28	Cyclo[cd]pyrene	0.0390

Table 2: List of PAH species in the nucleation and surface adsorption

$$\begin{aligned}
&\mathrm{C_{soot}}\cdot + \mathrm{H} \quad \rightarrow \quad \mathrm{C_{soot}} - \mathrm{H}\\
&\mathrm{C_{soot}}\cdot + \mathrm{C_2H_2} \quad \rightarrow \quad \mathrm{C_{soot}} - \mathrm{H} + \mathrm{H}\\
&\mathrm{C_{soot}}\cdot + \mathrm{O_2} \quad \rightarrow \quad 2\mathrm{CO} + \mathrm{products}\\
&\mathrm{C_{soot}} + \mathrm{H} + \mathrm{OH} \quad \rightarrow \quad \mathrm{CO} + \mathrm{products}\\
&\mathrm{C_{soot}} - \mathrm{H} + \mathrm{CH_3} \quad \Leftrightarrow \quad \mathrm{C_{soot}}\cdot + \mathrm{CH_4}\\
&\mathrm{C_{soot}} - \mathrm{H} + \mathrm{C_3H_3} \quad \Leftrightarrow \quad \mathrm{C_{soot}}\cdot + \mathrm{C_3H_4}\\
&\mathrm{C_{soot}} - \mathrm{H} + \mathrm{C_2H} \quad \Leftrightarrow \quad \mathrm{C_{soot}}\cdot + \mathrm{C_2H_2}
\end{aligned} \tag{9}$$

A complete list of surface reaction rates of the enhanced HACA mechanism is in Reference [37]. In addition, all PAH molecules in Table 2 can also condense onto the surface of a soot particle with the same collision efficiency γ_i (Table 2). The rate of increase in soot mass per surface area (in $[\mathrm{kg/m^2{-}m^3}]$) due to PAH adsorption is modelled as

$$\dot{R}(\mathrm{PAH}) = \sum_i \gamma_i \sqrt{\frac{R_\mathrm{J} T}{2\pi M_i}} [\mathrm{PAH}_i] Mc_i, \tag{10}$$

where Mc_i (in [kg/kmol]) is the carbon weight per mole for PAH_i. The surface growth rate is comprised of the HACA mechanism and the PAH adsorption process

$$G(v) = \frac{A_\mathrm{s}(v)}{\rho_\mathrm{s}} \left[\dot{R}(\mathrm{HACA}) + \dot{R}(\mathrm{PAH})\right], \tag{11}$$

where $\dot{R}(\mathrm{HACA})$ donates the surface-specific soot growth rate of the HACA mechanism and $\rho_\mathrm{s} = 1800\,\mathrm{kg/m^3}$ is the density of solid soot. Within an aggregate, neighbouring primary particles are assumed to be in point contact such that the surface area $A_\mathrm{s}(v)$ of an aggregate is estimated as [71]

$$A_\mathrm{s}(v) = A_\mathrm{p,a} N_\mathrm{p}(v) \left(1 - \phi C_\mathrm{ov} \left(1 - \frac{1}{N_\mathrm{p}(v)}\right)\right). \tag{12}$$

$$A_\mathrm{s}(v) = \begin{cases} \pi d_\mathrm{p}(v)^2, & N_\mathrm{p} < 1 \\ A_\mathrm{p,a}\left[1.72 N_\mathrm{p}(v)^{\frac{2}{3}} - 0.72\right], & 1 < N_\mathrm{p} < 10. \\ A_\mathrm{p,a} N_\mathrm{p}(v)\left(1 - \phi C_\mathrm{ov}\left(1 - \frac{1}{N_\mathrm{p}(v)}\right)\right), & N_\mathrm{p} > 10 \end{cases} \tag{13}$$

Here, $A_\mathrm{p,a}$ represents the surface area of a spherical particle with diameter $d_\mathrm{p,a}$, $C_\mathrm{ov} = 0.15$ is an overlapping parameter for neighbouring primary particles and ϕ is defined as the coordination number (number of contacts per primary particles), approximated as 1.3 for large $N_\mathrm{p}(v)$.

The collision kernel in the aggregation term for the free molecular and continuum regimes, respectively, is described according to [40]

$$\beta^{\mathrm{fm}}(v_i, v_j) = 2.2\sqrt{\frac{\pi k_{\mathrm{B}} T}{\rho_{\mathrm{s}}(v_i + v_j)}}\,(d(v_i) + d(v_j))^2\,, \tag{14}$$

$$\beta^{\mathrm{c}}(v_i, v_j) = \frac{2k_{\mathrm{B}}T}{3\mu}\left(\frac{C(v_i)}{d(v_i)} + \frac{C(v_j)}{d(v_j)}\right)(d(v_i) + d(v_j))\,, \tag{15}$$

where k_{B} is the Boltzmann's constant, $d(v)$ represents either the diameter of gyration of a fractal aggregate $d_{\mathrm{g}}(v)$ or the diameter of a spherical particle $d_{\mathrm{p}}(v)$ [50],

$$d_{\mathrm{g}}(v) = \begin{cases} d_{\mathrm{p}}(v), & N_{\mathrm{p}} < 1 \\ d_{\mathrm{p,a}}\left[-0.1067\, N_{\mathrm{p}}^3 + 0.6787\, N_{\mathrm{p}}^2 - 1.0219\, N_{\mathrm{p}} + 1.45\right], & 1 < N_{\mathrm{p}} < 4 \\ d_{\mathrm{p,a}}\left(0.1819\, N_{\mathrm{p}} - 4 + 0.6655\right), & 4 < N_{\mathrm{p}} < 10 \\ d_{\mathrm{p,a}}\left(\frac{N_{\mathrm{p}}}{k_{\mathrm{f}}}\right)^{\frac{1}{D_{\mathrm{f}}}}, & N_{\mathrm{p}} > 10 \end{cases} \tag{16}$$

In order to account for fractal shapes while maintaining a one-dimensional particle property space, we assume a soot particle to be spherical in shape if its volume is less than a critical value v_{c1}. On the other hand, it is assumed to be an aggregate consisting of several primary particles with identical volumes v_{c1} if the volume of this aggregate is greater than another critical value v_{c2}. In between these two limiting cases, soot particles may possess an intermediate shape whose morphological characteristics are detailed at the end of this section. We determined an average primary particle size of $d_{\mathrm{p,a}} = 30.8\,\mathrm{nm}$ based on TEM images of thermophoretically sampled soot particles in laminar ethylene flames [50]. For this reason, the first critical size is defined as the average size of primary particles $v_{\mathrm{c1}} = v_{\mathrm{p,a}}$; concomitantly, the second critical size is taken as $v_{\mathrm{c2}} = 10v_{\mathrm{p,a}}$ [71]. The number of primary particles in a fractal-like aggregate can be estimated from the power law [68].

The authors acknowledge that the physics of soot sub-models are not yet fully understood, The research of soot physics is still in progress and thus there is no consensus in the academic community. For example, this work did not consider the recent developments of soot physics, *i.e.*, reversible dimerisation in the nucleation and condensation process [72], internal oxidation of porous nanoparticles [73], and the soot surface reactivity affected by soot ageing [54]. However, these newly understood physics have not been popularised in the modelling studies of soot formation. In fact, we cannot find a universally acknowledged soot kinetics which is utilised by all modellers. However, people have agreed on the general physics of soot formation pathways: soot processes usually include nucleation (the dimerisation of PAHs by[36, 37]), surface growth (HACA mechanism by [38] or ARS aromatic site model by [39], and the PAH adsorptions), multi-regime coagulation/agglomeration by [40] and sintering by [41]. Many numerical studies employed this framework of soot formation. The soot dynamics with the set of empirical parameters for the based on the BPP mechanism (Blanquart et al. [64]) to model the soot formation process in an ethylene diffusion flame (Liu et al. [50]). The simulation results were validated with the line-of-sight soot volume fraction, elastic light scattering (ELS) signals and OH-Planarlaser-induced fluorescence (OH-PLIF) signals. Therefore, in this study, we still used the mechanism of Blanquart et al. [64] and the soot dynamics, called the original soot kinetics 'OR'; as a comparison, the sensitivity analysis of the soot kinetics concerning the contribution of PAHs and C_2H_2, is also conducted by tuning the nucleation, growth and PAH adsorption rates, with the absolute soot volume fraction basically unchanged, called the adjusted soot kinetics 'AD' and listed in Table 3. In addition, parameters studies of the soot kinetics on individual sub-processes of soot formation are also conducted: including increasing the nucleation rate by 10 times, the growth rate by 2 times and the adsorption rate by 10 times, and reducing the average primary particle size $d_{\mathrm{p,a}}$ to $24.0\,\mathrm{nm}$ [1]. These parameter studies are called the soot kinetics 'N10', 'G2','A10' and 'D24' respectively.

---

[1] In the dimethyl ether (DME) laminar coflow diffusion flame ([74]), the maximum soot volume fraction is less than $0.1\,\mathrm{PPM}$ and the average primary particle size is about (d_{p} = 8-10 nm). However, from the measurements of this study for the blended MD/DBE flames, the maximum soot volume fraction is about 1 - 2 PPM, but unfortunately, the average primary particle size was not measured and thus unavailable. The assumption of d_{p} =30.8nm in this work was estimated from a range of ethylene diffusion flames ([50, 75]) and the maximum soot volume fraction is about 5-10 PPM. But the authors believe that (d_{p}) in this study of the blended MD/DBE flames should probably more approximate to the ones in ethylene diffusion flames rather than the dimethyl ether (DME) laminar coflow diffusion flame ([74])Based on the leverage ratio, the authors also

Case	Abbreviation	Nucleation rate	Growth rate	PAH adsorption rate	Average primary particle $d_{\mathrm{p,a}}$
Original	OR	Eq. 8	$\dot{R}$ (HACA)	Eq.. 10	30.8 nm
Adjusted	AD	10 ×Eq.8	0.5 × $\dot{R}$(HACA)	10 ×Eq.10	30.8 nm
Parameter studies	N10	10 ×Eq.8	$\dot{R}$(HCCA)	Eq. 10	30.8 nm
	G2	Eq. 8	2 × $\dot{R}$(HACA)	Eq. 10	30.8 nm
	A10	Eq. 8	$\dot{R}$(HACA)	10 ×Eq.10	30.8 nm
	D24	Eq. 8	$\dot{R}$(HACA)	Eq. 10	24.0 nm

Table 3: Parameter studies on the soot kinetics

3. Simulation results and discussion

3.1. Temperature profiles

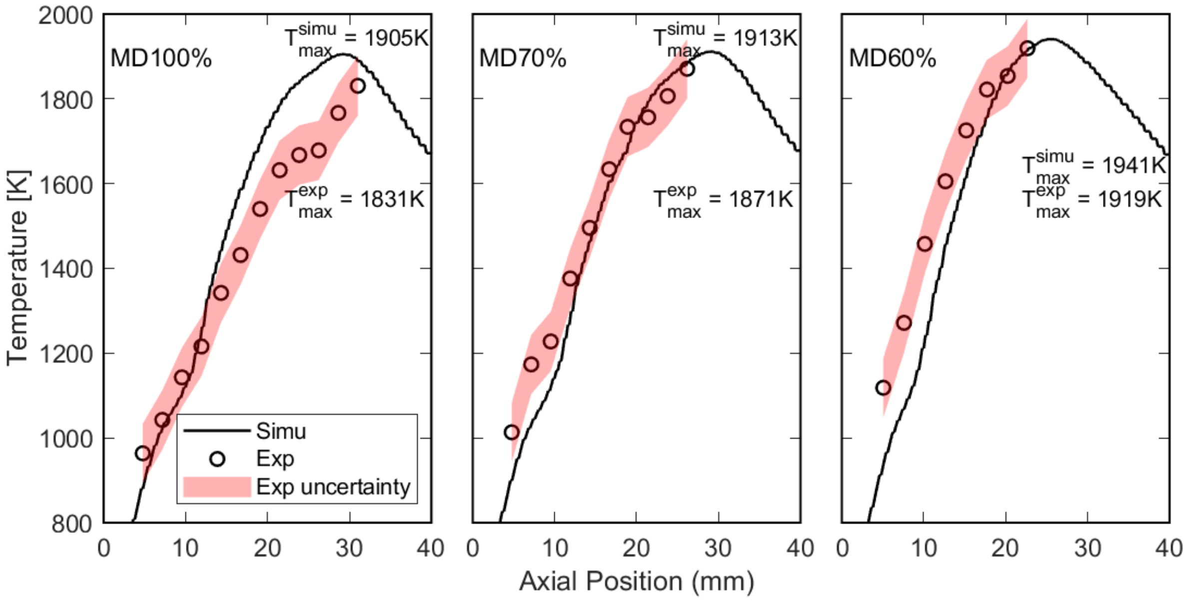

Figure 3: Temperature profiles along the centreline between the experiment [5] and simulations

Figure 3 compares the computed temperature profiles on the centreline with the measurements. For all three flames, in general, the predicted temperature profiles are basically in good agreement with the experimental data, and both the measurements and simulations indicate the highest maximum temperatures with 40% DBE addition. However, the numerical solutions present a smaller difference among the three flames: in the region from 20 mm to 30 mm HAB in the pure MD flame, the predicted temperature is around 100 K to 150 K higher than experimental results; for the 60% MD flame, the temperature is predicted lower prior to 10 mm HAB, which represents that the calculated heat release rate is slower than the experiment. As we found that the predicted soot volume fraction in the centreline is smaller than the measurement (See Sec 3.2), so that the predicted heat radiation is smaller than the reality. This can be a reason for the overprediction of the temperature on the centreline in the simulation for the case 100% MD.

---

conducted a parameter study on the average primary particle size with $d_{\mathrm{p}} = 24\,\mathrm{nm}$, labelled as 'Dp24'. However, the prediction also shows only the moderate difference of soot volume faction among the three flames with different DBE blend ratio.

3.2. Soot volume fraction

Figure 4a and 4b show contour plots of soot volume fraction in the experiment and simulation using the reduced combined mechanism CRA_DMBpp and the original soot kinetics 'OR'. The two graphs are displayed in the same unit [ppm], implying that the soot model predicts a correct magnitude of soot volume fraction. Essentially, the swallow-tail shape of the soot regions is correctly captured by the simulations. Although the prediction shows the emergence of soot at around 7 mm upstream than in the experiment, the positions of soot decaying are correctly predicted in the flames of 100% MD and 70% MD. Basically, the model has captured the reducing tendency of soot formation in the measurement as the DBE addition increases from 0% to 40%. Quantitatively, however, in Fig.5, the predicted integrated soot volume fraction on the centreline reduces by about 18%-20% as the mole fraction of DBE increases from none to 40%, compared to a much larger reduction of around 55% in the measurement. The simulation with the adjusted soot kinetics 'AD' shows the most soot loading reduction on the centreline as a result of the DBE addition, however, still much lower than the experimental results. In particular, the experiment shows that soot loadings reduce with the addition of DBE, with a significant reduction being as the fraction of MD decreases from 70% to 60%. In the simulation, however, soot is just slightly reduced with the DBE addition. Besides, in the experiment, the position where soot particles entirely burnt out moves forward by 10 mm in the 60% MD case, while in the simulation, it is nearly similar to the case of MD 100%. Another shortcoming is the fact that the sooty wings are overpredicted by the simulation while more soot forms around the centre region in the experiment.

As a comparison, Fig. 4c and 4d show the simulated soot volume fraction using the mechanism CRA_DMDlr (DLR) and the original soot kinetics 'OR', and using the mechanism CRA_DMBpp (BPP) and the adjust soot kinetics 'AD', respectively. The simulation with the CRA_DMDlr shows a larger soot volume fraction (with the legend scale 3 [ppm], see Fig. 4c) than with the CRA_DMBpp (with the legend scale 2 [ppm], see Fig. 4d). This is because the DLR mechanism predicts higher C_2H_2 concentration but a similar magnitude of C_3, C_4 and PAHs than the BPP mechanism (see Fig. 2c), and swallow-tails of the sooting region disappear all above $30\,\mathrm{mm}$ HAB. With the adjusted soot kinetics (CRA_DMBpp, AD, increasing the nucleation and PAH adsorption rate by 10 times while reducing the surface growth rate by twice, see Fig. 4d), the contribution by the PAHs is increased while the contribution by the C_2H_2 growth is reduced. As a result, in Fig. 4d, the soot formation on the flame centre is higher than the soot volume fraction in Fig. 4b. However, by changing the PAH chemical mechanism from BPP to DLR or the soot kinetics by balancing the contributions of PAHs and C_2H_2, the models still show an earlier emergence of soot formation upstream than in the experiment, less soot formation in the flame centre than on the flame wings and an underpredicted soot reducing capability of the DBE addition as compared to experimental data. Parameters studies on each individual sub-process of soot formation (nucleation rate, growth rate and adsorption rate, case 'N10','G2','A10') and the average primary particle size $d_{\mathrm{p,a}}$ (case 'D24') are shown Appedix E.

Figure 6a-c plot the radial profiles of the soot volume fraction at different heights above the burner in the three flames in the simulation using the CRA_DMBpp mechanism and in the experiment. The uncertainty range of the soot volume fraction measured by the 2D LII signals are estimated in Appendix F. To keep the figures easily readable, uncertainty bars of soot volume fraction are included only for the flame of pure MD. Considering the uncertainty in the measurements, the soot volume fraction is basically well predicted at $22.5\,\mathrm{mm}$ and $27.5\,\mathrm{mm}$ HAB for the 100% MD and 70% MD flames although it is fully overpredicted at $17.5\,\mathrm{mm}$. In the 60% MD flame, soot is completely burned out in the measurement while still exists in the simulation at $22.5\,\mathrm{mm}$ and $27.5\,\mathrm{mm}$ HAB heights.

Figure 6d-e also plot the profiles of soot volume fraction f_{v} on the centreline and on the pathline of the peak f_{v} along the axial direction. The soot is predicted to appear 5-10mm upstream than the measured data on the flame centre of the 100% MD and 70% MD flames, while decays 5-10mm downstream than the measured data. For the 60% MD flame, the soot volume faction is fully overpredicted on the flame centre and the peak pathline. On the whole, the model just shows the moderate difference of soot volume faction among the three flames with different DBE blend ratio.

3.3. Rates of the nucleation, growth, PAH adsorption and oxidation processes

Figure 7 presents and compare the contributions of the processes of the nucleation, growth, PAHs adsorption and oxidation of the blended cases with the chemical kinetics 'CRA_DMBpp' and the proposed soot kinetics 'OR'. Profiles at two heights ($17.5\,\mathrm{mm}$ and $22.5\,\mathrm{mm}$) and the flame centre are shown. In general, the nucleation rate, growth rate and the PAH adsorption rate are reduced as more DBE is blended into the MD medium while the oxidation rate

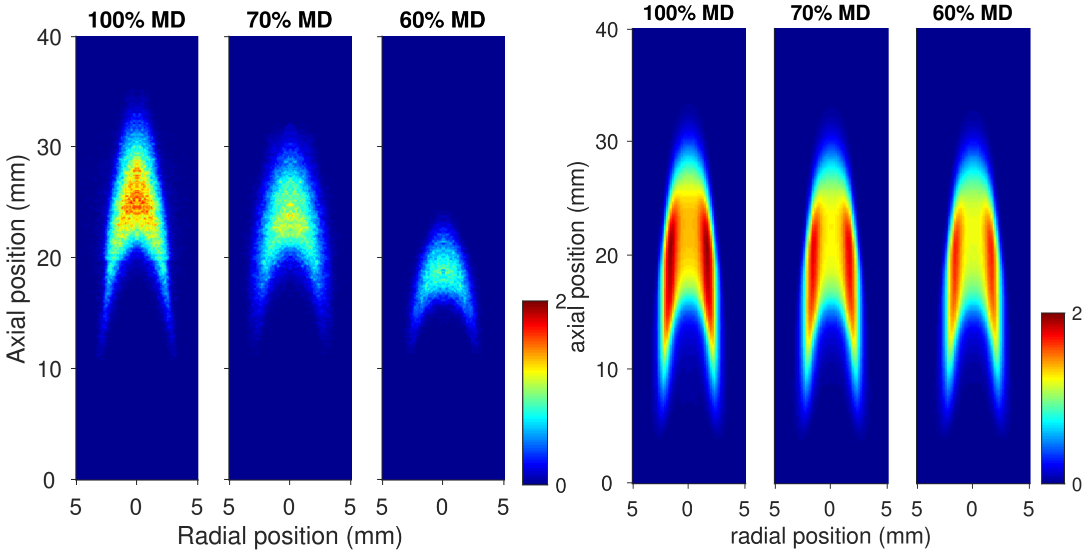

(a) Experiment results [ppm] **(b)** Simulation results [ppm] (CRA_DMBpp, OR)

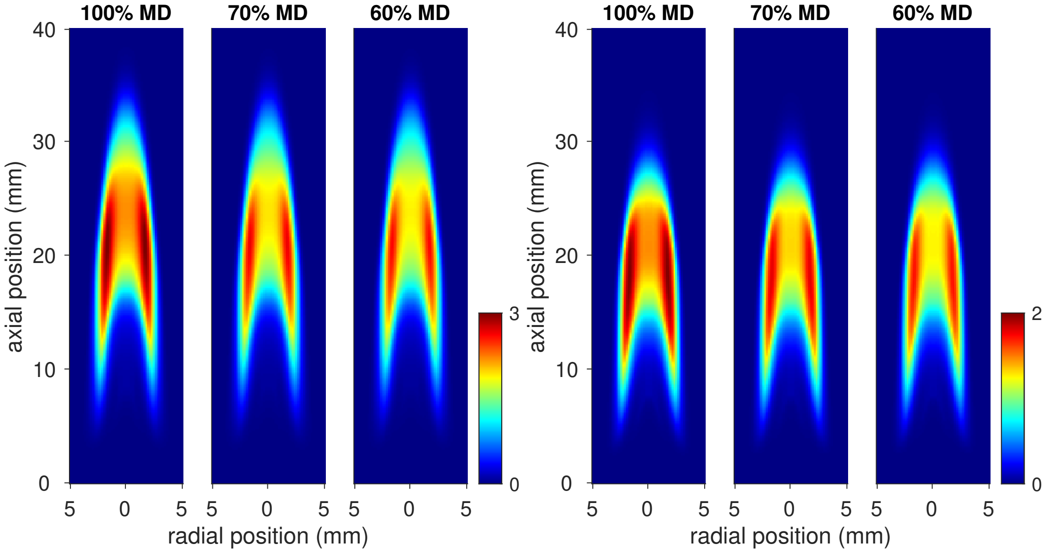

(c) Simulation results [ppm] (CR_DMDlr, OR) **(d)** Simulation results [ppm] (CRA_DMBpp, AD)

Figure 4: Comparisons of the soot volume fraction in contours between the experiment [5] and simulations

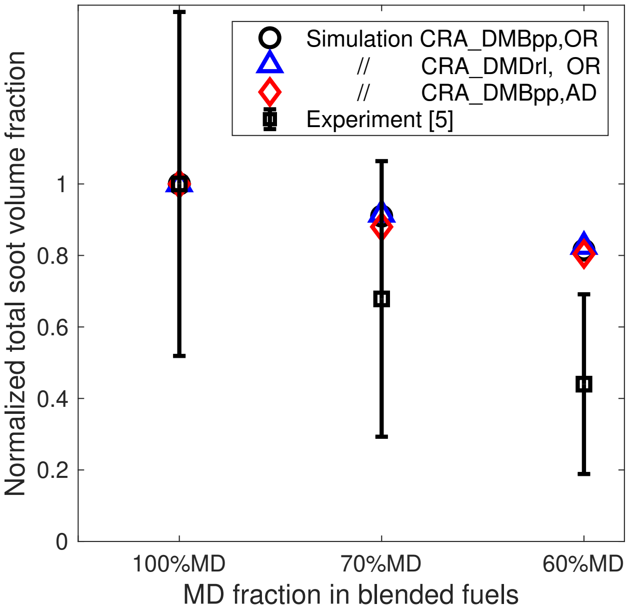

Figure 5: Normalised centreline soot loading as a function of the MD mole fraction between the experiment [5] and simulations

is increased. However, the difference of the soot sub-processes is quite small among the three blended cases, which determines the moderate difference of soot formation in the prediction.

3.4. Acetylene and PAH concentration

Figure 8 shows contour plots of mole fractions of C_2H_2 and PAH in the simulation of three flames, where the mole fraction of PAH accounts for the sum of species A_2, A_3 and A_4. The population balance modelling of soot formation is based on the PAH-HACA mechanism, therefore, the concentrations of C_2H_2 and PAH significantly affect soot formation. The C_2H_2 concentration does not change with the DBE addition, while the PAH concentration is suppressed by adding DBE in the fuel blends, around 15% quantitatively smaller on the centreline in the 60% MD flame than in the pure MD, according to Fig.9. As C_2H_2 contributes directly to the surface growth while the dimerisation of PAH lead to soot nucleation and adsorption, the soot reduction is mainly caused by a decreasing nucleation and adsorption rate. Here, the reason of only small difference of soot volume faction among the three flames with different MD-DBE mixture ratios in the simulations can be found: the insignificant difference of soot precursor species (C_2H_2 and PAH) in the combined MD-DBE-PAH mechanism.

Two different kinetics pathways: the combination of propargyl radicals and the reactions of C_4Hx species with acetylene, contribute to the cyclisation of the first aromatic rings (A1), which is a symbol to demonstrate the PAHs formation.

$$C_3H_4{-}p/C_3H_4{-}a/C_3H_3 + C_3H_3 = A_1(+H) \tag{17}$$
$$C_4H_4(C_4Hx) + C_2H_3(C_2H_2) = A_1(+H) \tag{18}$$

In Fig.9, the concentrations of species C_3H_4, C_3H_3 along the centreline show about 5% - 10% reduction as the DBE addition increases from none to 40%, which determines the reduced PAHs formation. For other species in the pathways of PAHs formation, the almost invisible difference can be found in the three flames. This also explains that differences in the PAHs concentration among the three flames are very small, thus leading to a smaller discrepancy of soot formation in the model than in the measurement.

Overall, the soot model can capture the reduction of soot formation by adding DBE into MD fuels. However, two main discrepancies between simulations and measurements arise, namely the early locations of soot occurrence and much slighter suppression of soot in the DBE-added cases.

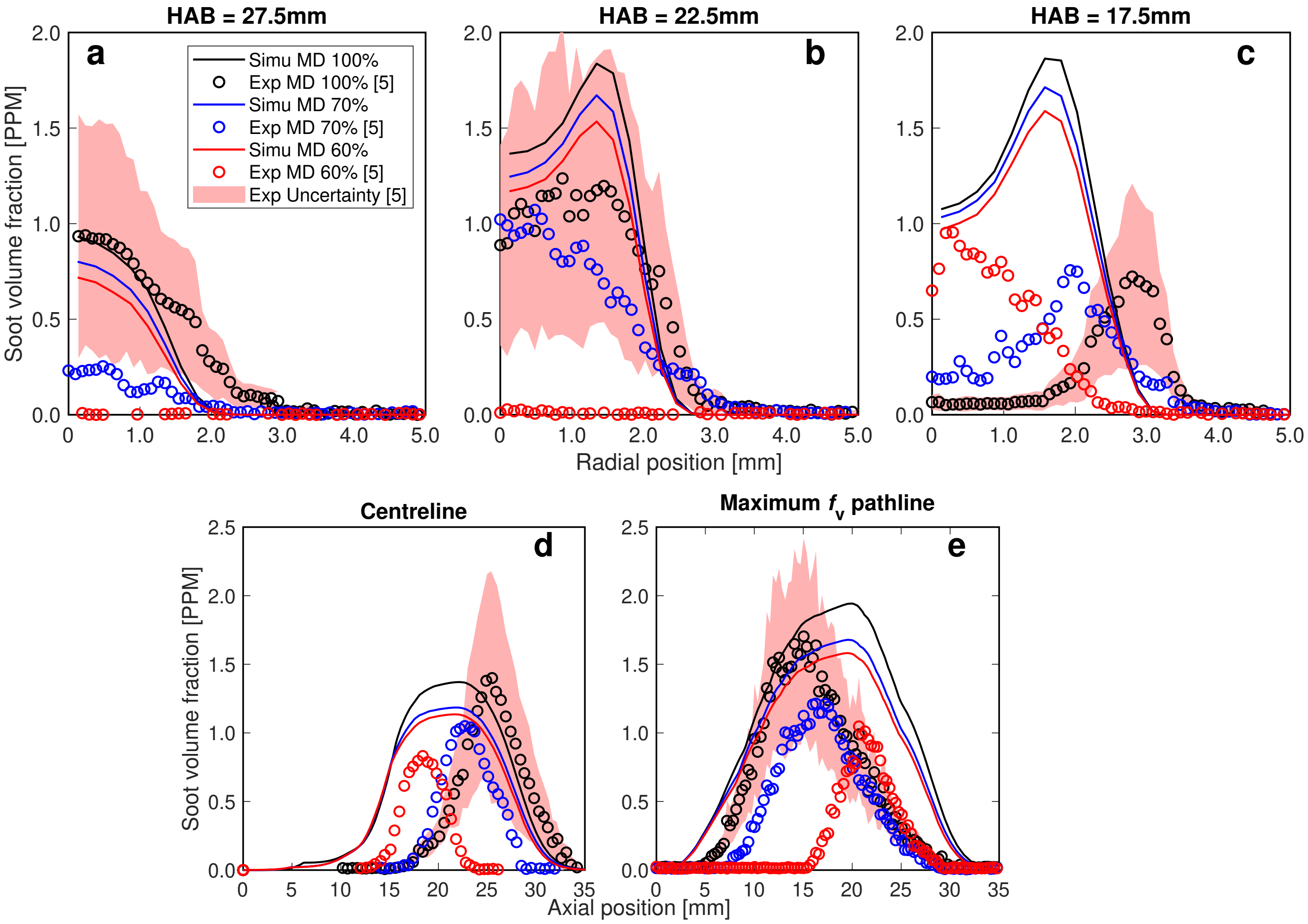

Figure 6: Radial profiles of soot volume fractions at different heights above the burner between the experiment [5] and the simulation based on the chemical mechanism 'CRA_DMBpp' and soot kinetics 'OR'

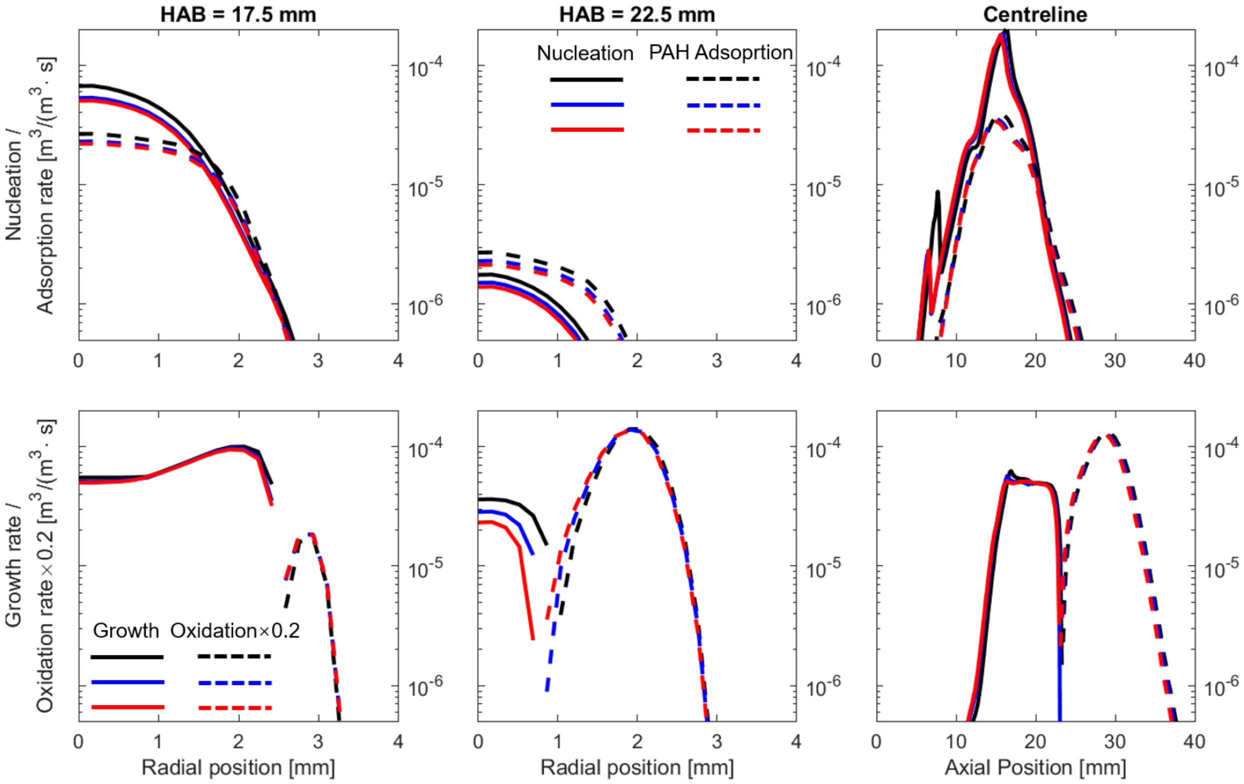

Figure 7: Radial profiles of the nucleation, surface growth, PAH adsorption and oxidation rates with the proposed chemical mechanism 'CRA_DMBpp' and soot kinetics 'OR'

The problem should mainly be attributed to the chemical mechanism: concentrations of soot precursor species (C_2H_2 and PAHs) and C2/C3/C4 molecules for PAH formation are similar in the three flames, although reda convincing procedure to combine the MD-DBE-PAH mechanism and validated it (CRA_DMBpp) in a perfect stirred reactor (see Fig.2) was conducted. In fact, the mechanisms CR_MD and CR_DM with the PAH sub-mechanism (not shown in the present paper) have been investigated, respectively, but neither of the combined MD-DBE-PAH mechanisms shows an evident difference between the combustion of MD and DBE in the laminar blended biodiesel flames, which is inadequate to model the suppression of soot formation by adding DBE into the blended fuel. In addition, the empirical parameters therein were calibrated based on ethylene diffusion flames [50]. The soot model could possibly be improved by adjustments based on soot morphological parameters in biodiesel fuel flames.

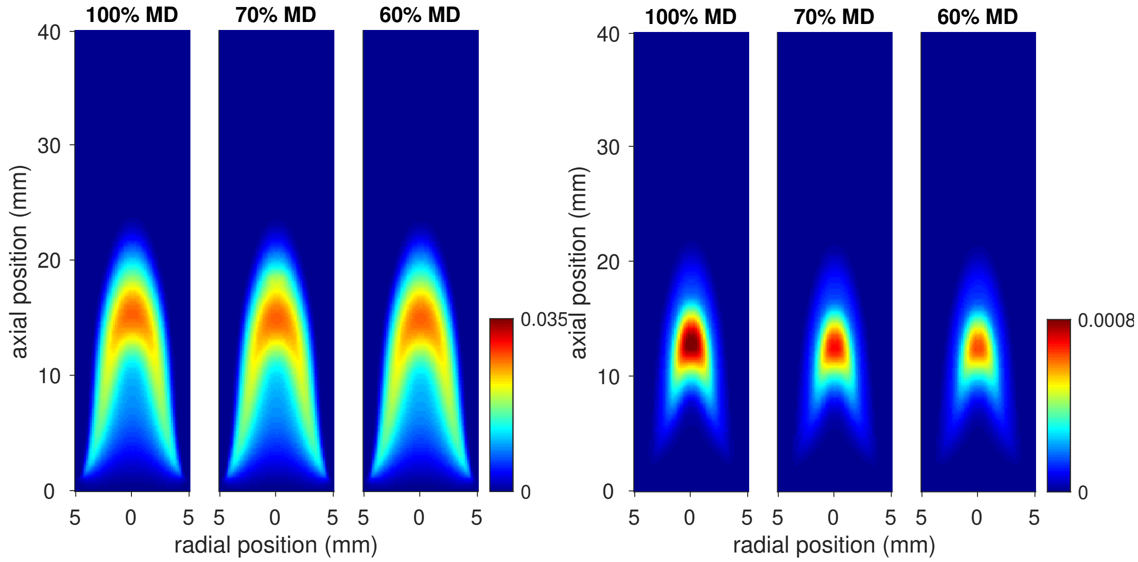

(a) C_2H_2 (mole fraction)

(b) PAH (mole fraction)

Figure 8: Contour plots of C_2H_2 and PAH in the simulation based on the chemical mechanism CRA_DMBpp

4. Conclusions

The objective of the present paper was to investigate the modelling of soot formation in laminar diffusion flames with different oxygenated surrogate blends of methyl decanoate (MD) and dibutyl ether (DBE). The main research question was whether the soot suppression in flames with different MD/DBE ratios that has been observed experimentally could be predicted by the model.

Three detailed chemical sub-mechanisms, the MD, the DBE and the PAH sub-mechanism, were reduced and combined as the MD-DBE-PAH mechanism with 530 species and 3437 reactions. In the spatially inhomogeneous combustion with fuels of heavy molecular weights, the mass diffusion term should be expressed in term of mole fraction in the transport equations of species and energy, while the molecular thermophoresis process and Dufour effect are negligible. The discretised population balance modelling of soot formation involves the processes of nucleation (PAH dimerisation), surface growth (HACA and PAH adsorption) and coagulation of spherical particles and fractal aggregates.

The predicted temperature profiles are basically in line with the experiment along the flame centrelines. In terms of the position and quantity of soot formation, the swallow-tail shape of the soot occurrence zone and the absolute value of soot production are correctly captured by the simulation. In terms of the soot suppression effect, the model has basically captured the reducing tendency of soot formation in the measurement as the DBE addition increases from 0% to 40%. Concentrations of PAHs and C3 species contributing to the formation of aromatic rings (PAHs) are reduced as the DBE addition is up to 40%, which is a leading cause of soot suppression. However, on the whole, the numerical solution featured much smaller differences than those observed in the experiment among laminar flames with different MD/DBE ratios. The reason has been found: the insignificant difference of soot precursor species (C_2H_2 and PAHs) in the combined MD-DBE-PAH mechanism, in which the main error is rooted in the combination process of sub-mechanisms. Given that so far there have been very few attempts to model soot formation in biodiesel flames, especially for the blends with different oxygenated fuels, the results are encouraging but future studies are warranted.

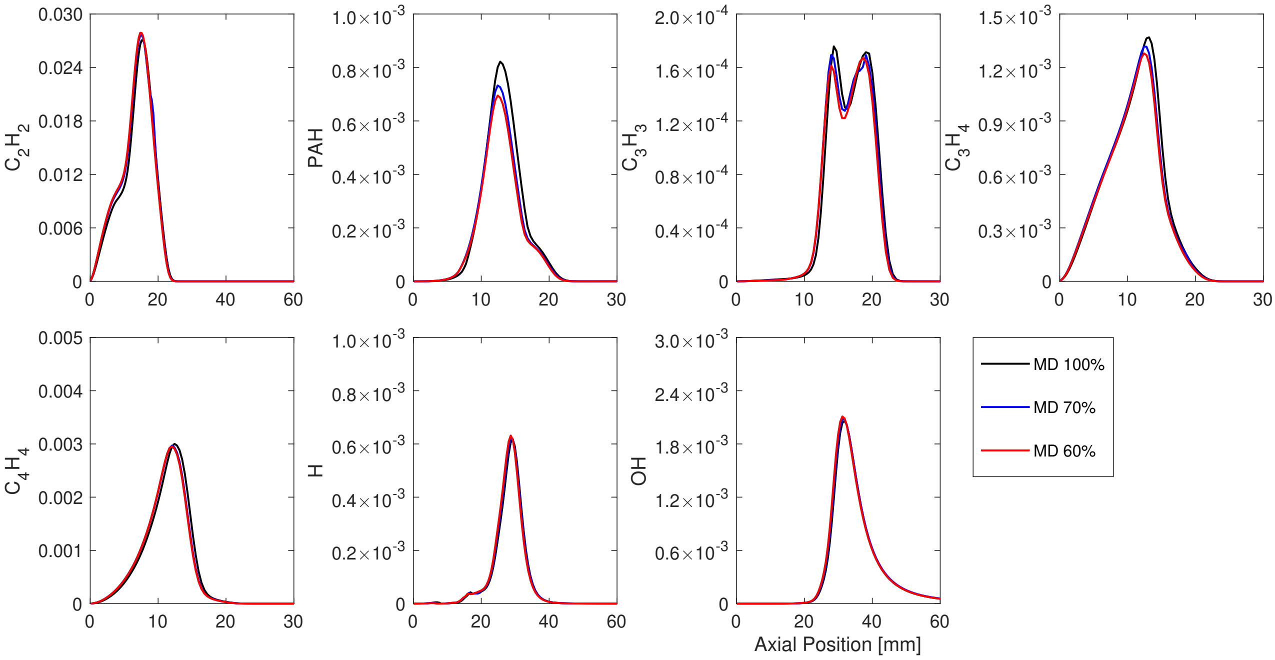

Figure 9: The profiles of concentrations of C2, C3, C4 and PAH species on the centreline

Acknowledgements

The authors gratefully acknowledge funding for the research and supercomputing time on ARCHER provided by the UK Engineering and Physical Sciences Research Council (EPSRC) under Grant Nos. EP/S012559/1 and EP/R029598/1.

References

[1] Q. Y. Feng, A. Jalali, A. M. Fincham, Y. L. Wang, T. T. Tsotsis, F. N. Egolfopoulos, Soot formation in flames of model biodiesel fuels, Combustion and Flame 159 (2012) 1876–1893.

[2] W. Merchan-merchan, S. McCollam, J. F. C. Pugliese, Soot formation in diffusion oxygen-enhanced biodiesel flames, Fuel 156 (2015) 129–141.

[3] J. Abboud, J. Schobing, G. Legros, et.al., Impacts of oxygenated compounds concentration on sooting propensities and soot oxidative reactivity: Application to diesel and biodiesel surrogates, Fuel 193 (2017) 241–253.

[4] M. R. Kholghy, J. Weingarten, A. D. Sediako, et.al., Structural effects of biodiesel on soot formation in a laminar coflow diffusion flame, Proceedings of the Combustion Institute 36 (2017) 1321–1328.

[5] Z. Gao, Z. Lei, X. Y. Zou, C. P. Liu, B. Tian, Z. Huang, Soot reduction effects of dibutyl ether (DBE) addition to a biodiesel surrogate in laminar coflow diffusion flames., Proceedings of the Combustion Institute 37 (2019) 1265-1272.

[6] A. Muelas, P. Remacha, J. Ballester, Droplet combustion and sooting characteristics of UCO biodiesel, heating oil and their mixtures under realistic conditions, Combustion and Flame 203 (2019) 190–203.

[7] G. Li, T. H. Lee, C. H. Zhang, Optical investigation on impacts of component ratio on spray, combustion and flame structure of isopropanol-butanol-ethanol (IBE)/diesel blends, Fuel 280 (2020) 118602.

[8] H. Q. Chu, Y. C. Ya, X. K. Nie, F. Qiao, J. Q. E, Effects of adding cyclohexane, n-hexane, ethanol, and 2,5-dimethylfuran to fuel on soot formation in laminar coflow n-heptane/iso-octane diffusion flame, Fuel 225 (2021) 120–135.

[9] W. Merchan, S. G. Sanmiguel, S. McCollam, Analysis of soot particles derived from biodiesels and diesel fuel air-flames, Fuel 102 (2012) 525–535.

[10] Z. Wang, L. Li, W. J. X., R. R. D., Effect of biodiesel saturation on soot formation in diesel engines, Fuel 175 (2016) 240–248.

[11] J. Kasumba, B. A. Holmén, Nonpolar organic compound emission rates for light-duty diesel engine soybean and waste vegetable oil biodiesel fuel combustion, Energy & Fuel 102 (2016) 9783–9792.

[12] J. Jeon, S. Park, Effect of injection pressure on soot formation/oxidation characteristics using a two-color photometric method in a compression-ignition engine fueled with biodiesel blend (B20), Applied Thermal Engineering 131 (2018) 284–294.

[13] R. L. Zhang, P. X. Pham, S. Kook, et. al., Influence of biodiesel carbon chain length on in-cylinder soot processes in a small bore optical diesel engine, Fuel 235 (2019) 1184–1194.

[14] Z. Liu, J. Liu, Effect of altitude conditions on combustion and performance of a turbocharged direct-injection diesel engine, Proceedings of the Institution of Mechanical Engineers, Part D: Journal of Automobile Engineering (2021) 1–12.

[15] Z. Liu, J. Liu, Experimental investigation of combustion characteristics of a single cylinder diesel engine at altitude, Journal of Energy Resources Technology 143 (2021) 102306.

[16] S. E. Iannuzzi, C. Barro, K. Boulouchos, J. Burger, Combustion behavior and soot formation/oxidation of oxygenated fuels in a cylindrical constant volume chamber, Fuel 167 (2016) 49–59.

[17] P. P. Desjardins, H. Pitsch, R. Malhotra, S. R. Kirby, A. L. Boehman, Structural group analysis for soot reduction tendency of oxygenated fuels, Combustion and Flame 154 (2008) 191–205.

[18] G. Knothe, C. A. Sharp, T. W. Ryan, Exhaust emissions of biodiesel, petrodiesel, neat methyl esters, and alkanes in a new technology engine, Energy & Fuel 154 (2006) 403–408.

[19] B. Jiang, D. Liu, Z. X. Lin, Soot particles diagnostics in ethylene inverse diffusion flame blending with biodiesel surrogates of saturated methyl butyrate and unsaturated methyl crotonate, Fuel Processing Technology 202 (2020) 49–59.

[20] C. McEnally, L. Pfefferle, The effects of dimethyl ether and ethanol on benzene and soot formation in ethylene nonpremixed flames, Proceedings of the Combustion Institute 31 (2007) 603–610.

[21] P. Y. Ni, D. P. Wei, X. L. Wang, D. P. Zhang, Z. Wang, Suppression of soot of a diesel engine fueled with biodiesel–diesel blend, Environmental Progress & Sustainable Energy 34 (2015) 282–288.

[22] A. Arad, E. Sher, G. Ebden, Modeling soot formation in diesel-biodiesel flames, Fuel 206 (2017) 437–452.

[23] H. An, W. M. Yang, A. Maghbouli, J. Li, S. K. Chou, K. J. Chua, J. X. Wang, L. Li, Numerical investigation on the combustion and emission characteristics of a hydrogen assisted biodiesel combustion in a diesel engine, Fuel 120 (2014) 186–194.

[24] J. Q. E, T. Liu, W. M. Yang, Y. W. Deng, J. K. Gong, A skeletal mechanism modeling on soot emission characteristics for biodiesel surrogates with varying fatty acid methyl esters proportion, Applied Energy 181 (2016) 322–331.

[25] M. Y. Xiao, H. F. Liu, X. J. Bi, H. Wang, C. F. Lee, Experimental and numerical investigation on soot behavior of soybean biodiesel under ambient oxygen dilution in conventional and low-temperature flames, Energy & Fuels 28 (2014) 2663–2676.

[26] F. Y. Zhao, W. M. Yang, D. Z. Zhou, W. B. Yu, J. Li, K. L. Tay, Numerical modelling of soot formation and oxidation using phenomenological soot modelling approach in a dual-fueled compression ignition engine, Fuel 188 (2017) 382–389.

[27] X. W. Cheng, H. K. Ng, S. Y. Gan, J. H. Ho, K. M. Pang, Numerical analysis of the effects of biodiesel unsaturation levels on combustion and emission characteristics under conventional and diluted air conditions, Energy & Fuel 32 (2018) 8392–8410.

[28] X. W. Cheng, S. Y. Gan, H. K. Ng, A numerical study on the quasi-steady spray and soot characteristics for soybean methyl ester and its blends with ethanol using CFD-reduced chemical kinetics approach, Energy 200 (2020) 117540.

[29] K. M. Pang, N. Karvounis, J. H. Walther, J. Schramm, Numerical investigation of soot formation and oxidation processes underlarge two-stroke marine diesel engine-like conditions using integrated CFD-chemical kinetics, Applied Energy 169 (2016) 874–887.

[30] X. L. Liu, H. Wang, M. F. Yao, Experimental and modeling investigations on soot formation of ethanol, n-butanol, 2,5-dimethylfuran, and biodiesel in diesel engines, Energy & Fuel 31 (2017) 12108–12119.

[31] Z. X. Xu, X. B. Duan, Y. Q. Liu, B. L. Deng, J. P. Liu, Spray combustion and soot formation characteristics of the acetone-butanol-ethanol/diesel blends under diesel engine-relevant conditions, Fuel 280 (2020) 118483.

[32] Z. Petranović, T. Bešenić, M. Vujanović, N. Duić, Modelling pollutant emissions in diesel engines, influence of biofuel on pollutant formation, Journal of Environmental Management 203 (2017) 1038–1046.

[33] N. H. Qamar, Z. T. Alwahabi, Q. N. Chan, G. J. Nathan, D. Roekaerts, K. D. King, Soot volume fraction in a piloted turbulent jet non-premixed flame of natural gas, Combustion and Flame 156 (2009) 1339–1347.

[34] M. Köhler, K. P. Geigle, B. M. Crosland, K. A. Thomson, G. J. Smallwood, Sooting turbulent jet flame: characterization and quantitative soot measurements, Applied Physics B 104 (2011) 409–425.

[35] P. M. Mandatori, Ö. Gülder, Soot formation in laminar ethane diffusion flames at pressures from 0.2 to 3.3 Mpa, Proceedings of the Combustion Institute 33 (2011) 577–584.

[36] G. Blanquart, H. Pitsch, A joint volume-surface-hydrogen multi-variate model for soot formation, in: H. Bockhorn, A. D'Anna, A. F. Sarofim, H. Wang (Eds.), Combustion Generated Fine Carbonaceous Particles, KIT Scientific Publishing, Karlsruhe, 2009, pp. 437–463.

[37] Y. Wang, A. Raj, S. H. Chung, Soot modeling of counterflow diffusion flames of ethylene-based binary mixture fuels, Combustion and Flame 162 (2015) 586–596.

[38] J. Appel, H. Bockhorn, M. Frenklach, Kinetic modeling of soot formation with detailed chemistry and physics: laminar premixed flames of C2 hydrocarbons, Combustion and Flame 121 (2000) 122–136.

[39] A. Raj, M. Sander, V. Janardhanan, M. Kraft, A study on the coagulation of polycyclic aromatic hydrocarbon clusters to determine their collision efficiency, Combustion and Flame 157 (2010) 523–534.

[40] S. Vemury, S. E. Pratsinis, Self-preserving size distributions of agglomerates, Journal of Aerosol Science 26 (1995) 175–185.

[41] B. X. Sun, S. Rigopoulos, A. X. Liu, Modelling of soot aggregation and sintering with a two-population balance equation model and a conservative finite volume method, Combustion and Flame (2021).

[42] M. K. Tran, D. Dunn-Rankin, T. K. Pham, Characterizing sooting propensity in biofuel-diesel flames, Combustion and Flame 159 (2012) 2181–2191.

[43] R. Lemaire, S. Bejaoui, E. Therssen, Study of soot formation during the combustion of diesel, rapeseed methyl ester and their surrogates in turbulent spray flame, Fuel 107 (2013) 147–161.

[44] C. Chong, S. Hochgreb, Study of soot formation during the combustion of diesel, rapeseed methyl ester and their surrogates in turbulent spray flame, Combustion Science Technology 184 (2012) 1093–1107.

[45] B. Tian, A. X. Liu, C. T. Chong, L. Fan, S. Y. Ni, J.-H. Ng, S. Rigopoulos, K. H. Luo, S. Hochgreb, Experimental and numerical study on soot formation in laminar diffusion flames of biodiesels and methyl esters, Proceedings of the Combustion Institute (2020).

[46] J. Brakora, R. Y., R. D. Reita, J. McFarlane, C. S. Daw, Development and validation of a reduced reaction mechanism for biodiesel fueled engine simulations, in: SAE, 2008, pp. 675–702.

[47] J. Yu, J. Y., X. Gou, Surrogate fuel formulation for oxygenerated and hydrocarbon fuels by using the molecular structures and functional groups, Fuel 166 (2015) 211–218.

[48] A. Li, L. Zhu, Y. Mao, J. Q. Zhai, D. Han, x. C. Lu, Z. Huang (????).

[49] E. Y. K. Yee, Numerical Simulation of Soot in Laminar Flames, Ph.D. thesis, University of Cambridge, UK, 2016.

[50] A. X. Liu, C. E. Garcia, F. Sewerin, B. A. O. William, S. Rigopoulos, Population balance modelling and laser diagnostic validation of soot particle evolution in laminar ethylene diffusion flames, Combustion and Flame 221 (2020) 384–400.

[51] F. Liu, X. He, X. Ma, Q. Zhang, M. J. Thomson, H. Guo, G. J. Smallwood, S. Shuai, J. Wang, An experimental and numerical study of the effects of dimethyl ether addition to fuel on polycyclic aromatic hydrocarbon and soot formation in laminar coflow ethylene/air diffusion flames, Combustion and Flame 158 (2011) 547–563.

[52] F. Liu, S. B. Dworkin, M. J. Thomson, G. J. Smallwood, Modeling DME addition effects to fuel on pah and soot in laminar coflow ethylene/air diffusion flames using two pah mechanisms, Combustion Science and Technology 184 (2012) 966–979.

[53] H. F. Jin, A. Cuoci, A. Frassoldati, T. Faravelli, Y. Z. Wang, Y. Y. Li, Experimental and kinetic modeling study of PAH formation in methane coflow diffusion flames doped with n-butanol, Combustion and Flame 161 (2014) 657–670.

[54] A. Khosousi, F. S. Liu, S. B. Dworkin, N. A. Eaves, M. J. Thomson, X. He, Y. J. Dai, F. S. Gao, Y. L. adn Liu, S. J. Shuai, J. X. Wang, Experimental and numerical study of soot formation in laminar coflow diffusion flames of gasoline/ethanol blends, Combustion and Flame 162 (2015) 3925–3933.

[55] M. R. Kholghy, J. Weingarten, M. J. Thomson, A study of the effects of the ester moietyon soot formation and species concentrations in a laminar coflow diffusion flame of a surrogate for B100 biodiesel, Proceedings of the Combustion Institute 35 (2015) 905–912.

[56] A. Liu, S. Rigopoulos, A conservative method for solution of the population balance equation, and application to soot formation, Combustion and Flame 205 (2019) 506–521.

[57] W. P. Jones, F. di Mare, A. J. Marquis, LES-BOFFIN: user's guide, 2002.

[58] B. Tian, Y. Gao, S. Balusamy, S. Hochgreb, High spatial resolution laser cavity extinction and laser-induced incandescence in low-soot-producing flames, Applied Physics B 120 (2015) 469-487.

[59] Theory Manual: Chemkin-Pro for Reaction Design, San Diego, 2008.

[60] A. Kronenburg, R. W. Bilger, J. H. Kent, Modeling soot formation in turbulent methane–air jet diffusion flames, Combustion and Flame 121 (2000) 24–40.

[61] http://www.sandia.gov/tnf/radiation.html, 2003.

[62] S. M. Sarathy, M. J. Thomson, W. J. Pitz, An experimental and kinetic modeling study of methyl decanoate combustion, Proceedings of the Combustion Institute 33 (2011) 399–405.

[63] L. Cai, A. Sudholt, D. J. Lee, F. N. Egolfopoulos, H. Pitsch, C. K. Westbrook, S. M. Sarath, Chemical kinetic study of a novel lignocellulosic biofuel: Di-n-butyl ether oxidation in a laminar flow reactor and flames, Combustion and Flame 161 (2014) 798–809.

[64] G. Blanquart, P. Pepiot-Desjardins, H. Pitsch, Chemical mechanism for high temperature combustion of engine relevant fuels with emphasis on soot precursors, Combustion and Flame 156 (2009) 588–607.

[65] S. B. Dworkin, Q. Zhang, M. J. Thomoson, S. N. A., U. Riedel, Application of an enhanced PAH growth model to soot formation in a laminar coflow ethylene/air diffusion flame, Combustion and Flame 158 (2011) 1682–1695.

[66] N. A. Slavinskaya, P. Frank, A modelling study of aromatic soot precursors formation in laminar methane and ethene flames, Combustion and Flame 156 (2009) 1705–1722.

[67] H. M. Hulburt, S. Katz, Some problems in particle technology: A statistical mechanical formulation, Chemical Engineering Science 19 (1964) 555–574.

[68] S. K. Friedlander, Smoke, Dust and Haze, second ed., Oxford University Press, Oxford, New York, 2000. ISBN 0-19-512999-7.

[69] R. Kosfeld, The physics of polymers, concepts for understanding their structures and behavior, Int. J. Res. Phys. Chem. Chem. Phys. 206 (1998) 274–276.

[70] S. Suzuki, K. Kuwana, R. Dobashi, Effect of particle morphology on thermophoretic velocity of aggregated soot particles, Int. J. Heat Mass Tran. 52 (2009) 4695–4700.

[71] A. M. Brasil, T. L. Farias, M. G. Carvalho, A recipe for image characterization of fractal-like aggregates, Journal of Aerosol Science 30 (1999) 1379–1389.

[72] N. Eaves, S. Dworkin, M. Thomson, Assessing relative contributions of pahs to soot mass by reversible heterogeneous nucleation and condensation, Proceedings of the Combustion Institute 36 (2017) 935–945.

[73] G. A. Kelesidis, S. E. Pratsinis, Estimating the internal and surface oxidation of soot agglomerates, Combustion and Flame 209 (2019) 493–499.

[74] T. Li, T. Mitra, C. Chu, Y. Yuan, M. Thomson, Investigation of pah and soot formation in a dimethyl ether (DME) laminar coflow diffusion flame, Combustion and Flame 223 (2021) 437–449.

[75] K. Tian, K. A. Thomson, F. Liu, D. R. Snelling, Determination of the morphology of soot aggregates using the relative optical density method for the analysis of tem images, Combustion and Flame 144 (2006) 782–791.

[76] A. D'Alessio, A. Di Lorenzo, F. Beretta, C. Venitozzi, Optical and chemical investigations on fuel-rich methane-oxygen premixed flames at atmospheric pressure, Symposium (International) on Combustion 14 (1973) 941–953.

Appendix A Target species and corresponding relative tolerance errors in the chemistry reduction for the MD and the DBE mechanisms, using DRGEPSA algorithm

relative tolerance	target species for chemistry reduction
10%	C_2H_2 C_3H_3 DBE CO_2 CO H MD O_2 OH Temperature
15%	C_2H_3 C_3H_2 C_3H_4-a C_3H_4-p C_3H_5-a C_4H_4 C_4H_5-n
20%	C C_2H C_2H_3CHO C_2H_5 C_2H_6 C_3H_5-s C_3H_5-t C_3H_5O C_3H_6 C_3H_8 C_3H_6 CH CH_2CHO CH_2CO CH_2O CH_2OH CH_3CHO CH_3O CH_3O_2 CH_3OH CH_4 H_2 H_2CC H_2O H_2O_2 HCCO HCCOH HCO HO_2 iC_3H_5OH iC_3H_7 iC_4H_7 iC_4H_7O iC_4H_8 nC_3H_7 nC_3H_7CHO nC_3H_7O O

Appendix B In the CRA_DMBpp mechanism, the common chemical reactions among three sub-mechanisms F_M [62], F_D [63] and PAH [36] whose rate constants are succeeded from F_M or PAH instead of F_D

$C_2H_2 + H + M = C_2H_3 + M$	F_M
$C_2H_2 + O = CH_2 + CO$	PAH
$C_2H_2 + O = HCCO + H$	PAH
$C_2H_2 + OH = C_2H + H_2O$	F_M
$C_2H_2 + OH = CH_2CO + H$	F_M
$C_3H_6 + OH = C_3H_5-a + H_2O$	F_M
$C_3H_4-a + H = C_3H_5-a$	F_M
$C_3H_4-p = C_3H_4-a$	F_M
$C_3H_4-a + H = C_3H_3 + H_2$	F_M
$C_3H_4-p + H = C_3H_4-a + H$	PAH
$C_3H_3 + H = C_3H_4-a$	F_M
$C_3H_3 + H = C_3H_2 + H_2$	PAH

Appendix C Evaluation of additional diffusion terms in transport equations

The molecular weights of gasoline, diesel and biodiesel fuels, are usually in the range of 100 - 250. The transport equations of species and energy are usually numerically implemented in a simple format, by neglecting three additional terms (the effect of molecular weight, thermophoresis and Dufour effect). In this section, these diffusion terms in the species transport equations and the energy equation are evaluated in the laminar flame with pure MD fuel. From Fig.C.1a, the transport equations with respect to H and MD species, respectively, are selected to evaluate the difference of three diffusion components since the molecules H and MD are of the minimum and maximum molecular weights, respectively in the flame.

Three diffusion components, ordinary diffusion term, effect of the average molecular weight and thermophoresis, are marked as 'O', 'M' and 'T' in the legend. The ordinary term oscillates in the region where the species concentrations increase and decrease (the right part of Fig.C.1b). By comparison, the molecular weight term and thermophoresis are negligible in the transport equation of H, but the molecular weight term in the transport equation of MD is about 1/5 of the ordinary term in the transport equation of MD. Therefore, for the transport equations of heavy molecules, the molecular weight term in Eq. 2 should be included.

On the other hand, in Fig.C.1c, additional diffusion components account rednotably in the energy equation, compared with the ordinary diffusion term. 'M', 'T', 'D', 'O' in the legend represent the term of molecular weight effect, thermophoresis, Dufour effect and the ordinary diffusion term, respectively. The term of molecular weight effect is a

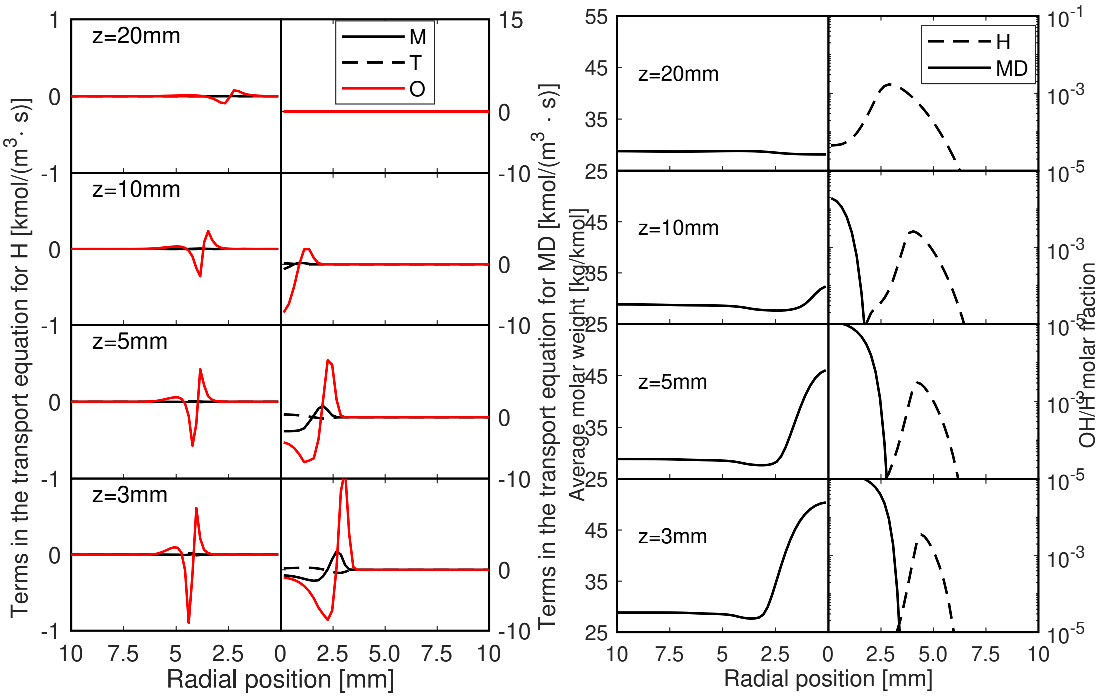

(a) Diffusion terms in the transport equations of species

(b) Local average molecular weight and concentrations of H and MD

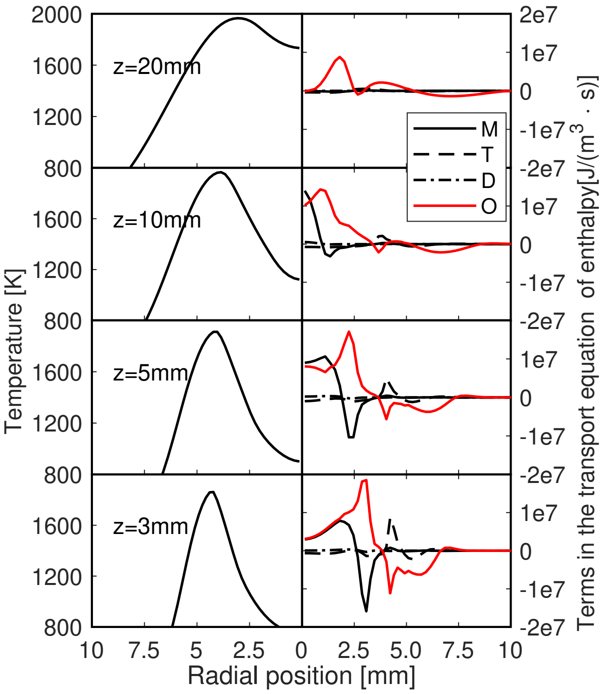

(c) Temperature and diffusion terms in the transport equation of energy

Figure C.1: Comparison of diffusion terms in the transport equations of species and energy positive value on the centreline close to the jet burner until 10 mm above, corresponding to the region of high average molecular weight in Fig.C.1b. Then the effect becomes negative in the radial direction due to the varying average molecular weight, compensating the positive ordinary diffusion term. Around the reacting zone of peak temperature (the left column in Fig.C.1b) and species source (the right column of Fig.C.1b, thermophoresis effect contributes an opposite equivalence to the ordinary diffusion term, although the absolute values are minor compared with those around the centreline. Different from transport equations of species (Eq. 2), no source term exists in the energy equation in terms of total enthalpy. Therefore, the additional diffusion components largely affect the energy equation, thus the temperature field.

Figure C.2 compares the temperature profiles using four different expressions of transport equations: with full terms, the molecular weight term removed, the thermophoresis term removed, both terms of the molecular weight and thermophoresis removed. By removing the molecular weight term, the temperature has increased by 50 K - 100 K at $30\,\mathrm{mm}$ HAB downstream on the centreline and by around 50 K at $15\,\mathrm{mm}$ - $30\,\mathrm{mm}$ radial locations away from the centreline on different heights above the burner. But thermophoresis term makes no difference. Therefore, redthe mass diffusion term should be expressed in term of mole fraction in the transport equations of species and energy, while the molecular thermophoresis process and Dufour effect can be negligible.

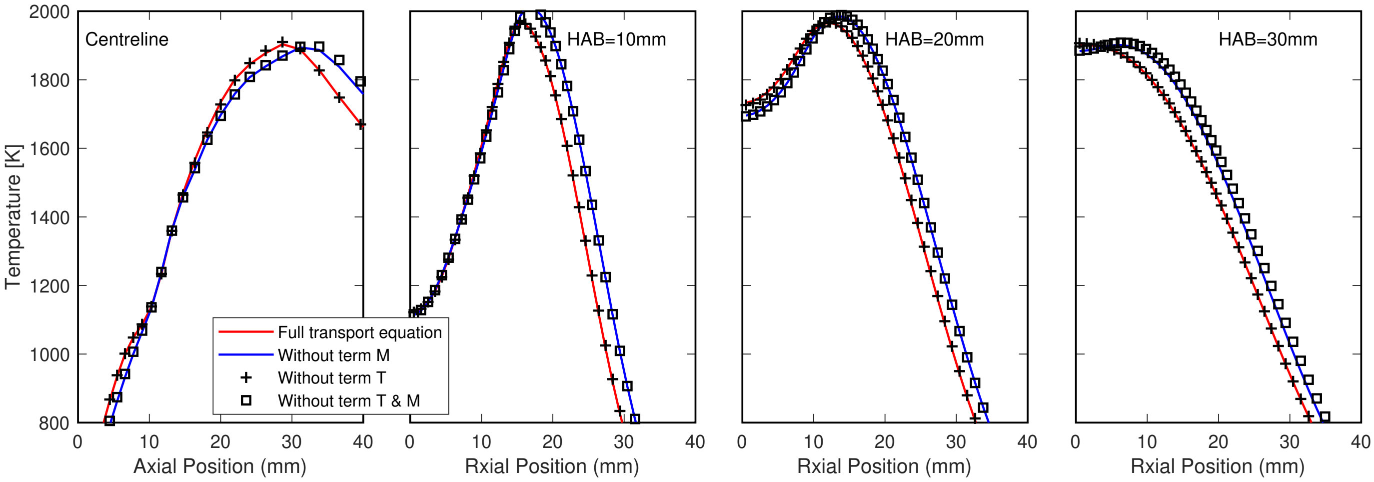

Figure C.2: Temperature profiles using different expressions in the transport equations

Appendix D Analysis on the diffusive and thermophoretic velocity of soot

As the effects of secondary diffusion terms in the transport equation of species and energy are elaborated in Appendix C, the effects of the soot diffusion and soot thermophoretic velocity will be discussed in this section. A detailed description on how the soot diffusivity and thermophoretic velocity were modelled is given.

The average diffusivity velocity and thermophoretic velocity of soot particles are displayed as

$$\overline{K_j} = \frac{\sum K_j(vn(v))}{\sum n(v)} \tag{D.1}$$

$$\overline{U_j^{\mathrm{T}}} = \frac{\sum U_j^{\mathrm{T}} vn(v)}{\sum n(v)} \tag{D.2}$$

Figure D.1a shows the contributions of the soot diffusion velocity and soot thermophoretic velocity on the flame centreline and at $17.5\,\mathrm{mm}$ and $27.5\,\mathrm{mm}$ height above the burner. The values of thermophoretic velocity are around 2 orders of magnitude lower than the bulk velocity while the diffusion velocity is around 3 orders of magnitude lower. Therefore, in Figure D.1b, by removing the diffusion velocity, the predicted soot volume fraction is not affected, while by removing soot thermophoretic velocity, the profile of soot volume fraction changes slightly, particularly at HAB = $17.5\,\mathrm{mm}$.

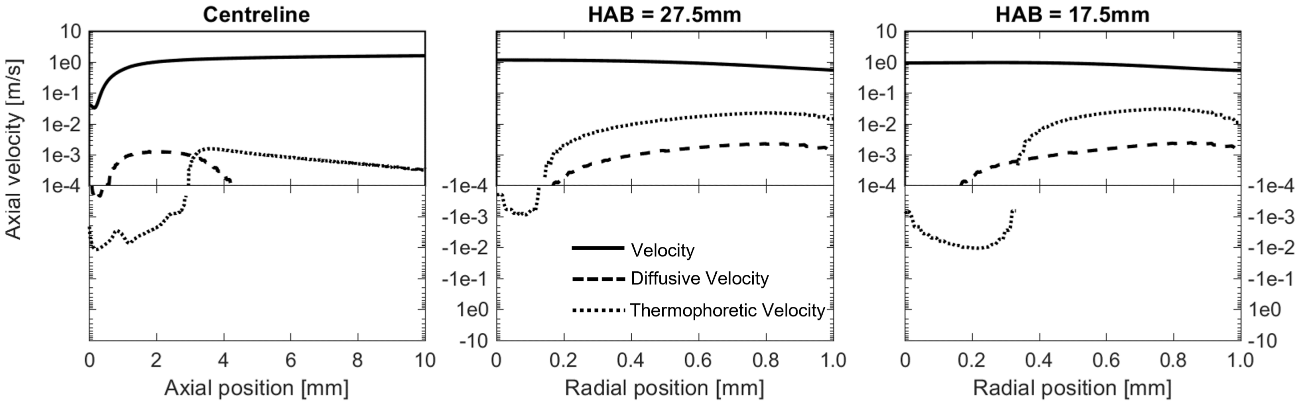

(a) Mass velocity, diffusive velocity and thermophoretic velocity of soot particles

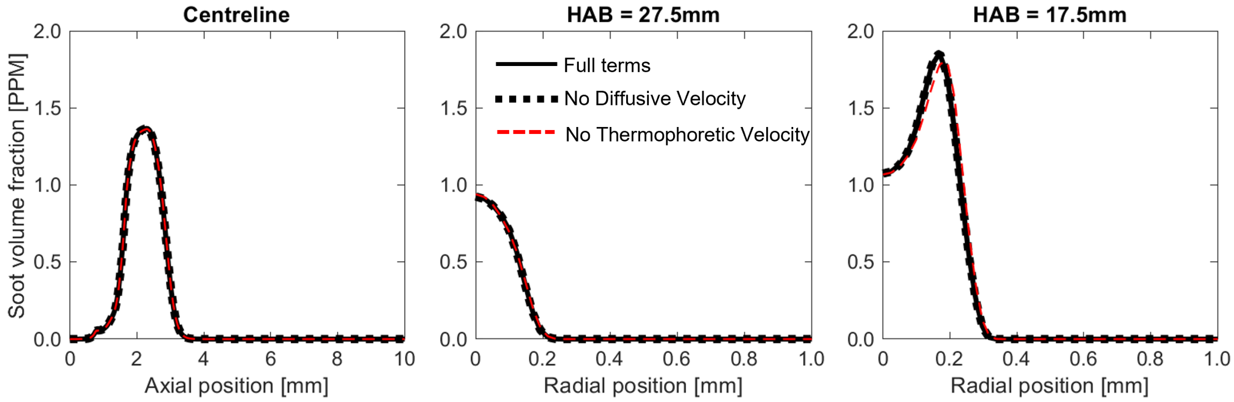

(b) Soot volume fraction for the cases with the full terms, no diffusive velocity and no thermophoretic velocity

Figure D.1: Effects of soot diffusional terms

Appendix E Parameter study of the nucleation rate, growth rate, adsorption rate and the average primary particle size in the proposed soot formation model

Parameters studies on each individual sub-process of soot formation (nucleation rate, growth rate and adsorption rate, case 'N10','G2','A10') and the average primary particle size $d_{\mathrm{p,a}}$ (case 'D24') are shown in this appendix.

Figure. E.1 shows the simulated soot volume fraction using different soot kinetics 'N10','G2','A10' and 'D24', respectively based on the mechanism CRA_DMBpp (BPP). By increasing the nucleation rate or surface growth rate, individually or reducing the assumed average primary particle size $d_{\mathrm{p,a}}$, the predicted absolute soot volume fraction has increased, comparing with the original soot kinetics 'OR' (see Fig. 4b. However, the models still show an earlier emergence of soot formation upstream than in the experiment, less soot formation in the flame centre than on the flame wings and an underpredicted soot reducing capability of the DBE addition as compared to experimental data (see Fig. 4a).

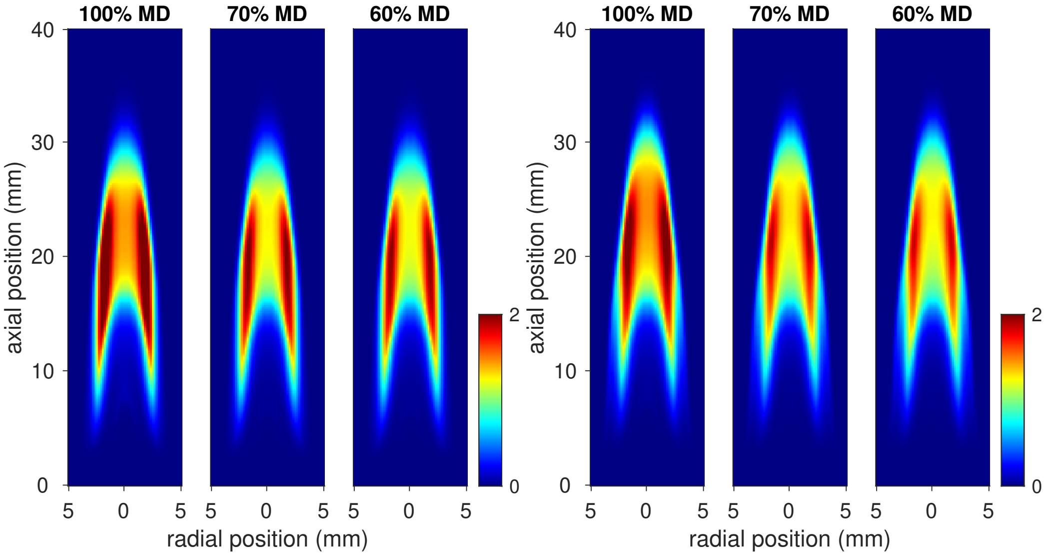

(a) Increasing the nucleation rate by 10 times (CR_DMBpp, N10)

(b) Increasing the growth rate by twice (CRA_DMBpp, G2)

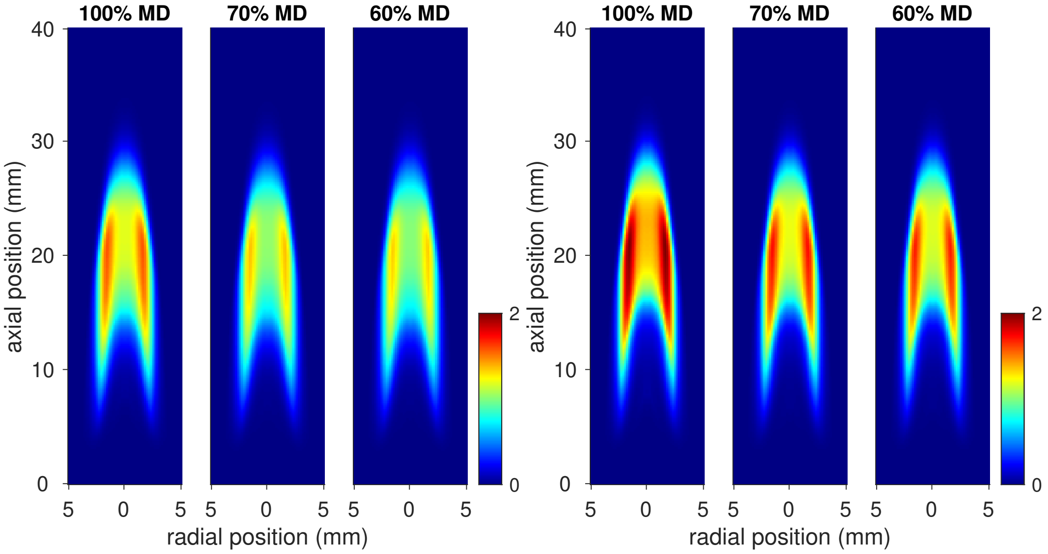

(c) Increasing the PAH adsorption rate by 10 times (CR_DMBpp, A10)

(d) Assuming the average primary particle size d_{p} = 24.0 nm (CRA_DMBpp, D24)

Figure E.1: Simulation results of contours plots of the soot volume fraction for the parameter study of the nucleation rate, growth rate, adsorption rate and the average primary particle size in the proposed soot formation model

Appendix F Uncertainty analysis of the local soot volume fraction by using LII measurements

In this study, the local soot volume fraction $f_\mathrm{v} =$ is determined by the 2D LII signals S_LII [5, 58],

$$f_\mathrm{v} = \frac{S_\mathrm{LII}}{K_\mathrm{LII}} \tag{F.1}$$

The calibration constant K_LII is the ratio of the mean collected LII signal at emission signal wavelength per unit soot extinction, and is obtained by connecting the measured extinction signals S_LII to the corresponding integrated soot volume fraction f_v, as follows,

Therefore, the calibration constant K_LII can be obtained using:

$$K_\mathrm{LII} = \frac{1}{\ln I_o - \ln I(0)} \frac{6\pi E(m)}{\lambda_\mathrm{e}} \int_{-\infty}^{+\infty} S_\mathrm{LII}(r)\mathrm{d}r \tag{F.2}$$

where I_o represents the intensity of the incident laser beam and $I(0)$ is the intensity of the transmitted beam passing the sooting flame centre. λ_e is the laser wavelength. $E(m)$ is the soot absorption function:

$$E(m) = -\mathrm{Im}\left(\frac{m^2-1}{m^2+2}\right) \tag{F.3}$$

where m is the complex index of refraction of soot. Based on Eq. F.1, the relative uncertainty of f_v is

$$\begin{aligned} \frac{\Delta f_\mathrm{v}}{f_\mathrm{v}} &= \frac{1}{f_\mathrm{v}}\left(\frac{\Delta S_\mathrm{LII}}{K_\mathrm{LII}} - \frac{S_\mathrm{LII}\Delta K_\mathrm{LII}}{K_\mathrm{LII}^2}\right) \\ &= \frac{\Delta S_\mathrm{LII}}{S_\mathrm{LII}} - \frac{\Delta K_\mathrm{LII}}{K_\mathrm{LII}} \end{aligned} \tag{F.4}$$

That is

$$\frac{|\Delta f_\mathrm{v}|}{f_\mathrm{v}} = \frac{|\Delta S_\mathrm{LII}|}{S_\mathrm{LII}} + \frac{|\Delta K_\mathrm{LII}|}{K_\mathrm{LII}} \tag{F.5}$$

The statistic uncertainty of the LII signals $\frac{|\Delta S_\mathrm{LII}|}{S_\mathrm{LII}}$ were obtained directly from the standard deviation through the statistical analysis of at least 40 LII images.

The systematic errors in K_KII mainly arises from the assumed value for $E(m)$. Tian et al. [58] collated values of m and $E(m)$ from previous investigations on smoking flames with various laser wavelengths and fuels. For a wavelength of about $632\,\mathrm{nm}$, the values of $E(m)$ were reported to range from 0.17 to 0.37. In this study, $E(m)$ is assumed to be 0.26, based on the estimated value of the index of refraction m = 1.57-0.56i ([76]). Hence,

$$\frac{|\Delta K_\mathrm{LII}|}{K_\mathrm{LII}} \approx \frac{|\Delta E(m)|}{E(m)} = 0.42 \tag{F.6}$$

The error bar of f_v has been corrected in Figure 5 and 6, considering both the statistic uncertainty of the 2D LII signals S_LII and the systematic uncertainty of $E(m)$.